Doubly Cabibbo Suppressed D^+ Decays and Singly Cabibbo Suppressed D_s^+ Decays in 220 GeV $\gamma + p$ Interactions.

By

Gary P. Grim

August 1995

DISSERTATION

Submitted in partial satisfaction of the requirements for the degree of

DOCTOR OF PHILOSOPHY

in

Physics

in the

GRADUATE DIVISION

of the

UNIVERSITY OF CALIFORNIA

DAVIS

Approved:

. . . . . .

. . . . . .

. . . . . .

Abstract

Branching ratios and upper limits at 90% confidence level for D^+ and $D_s^+ \to K^+\pi^-\pi^+$ decays collected by Fermilab experiment E-687 are reported. The D^+ results are: , $(D^+ \to K^+\pi^-\pi^+)/$, $(D^+ \to K^-\pi^+\pi^+) = (7.2\pm2.3\pm1.7)\times10^{-3}$, , $(D^+ \to K^{*0}(892)\pi^+)/$, $(D^+ \to K^-\pi^+\pi^+) < 0.0021$, and , $(D^+ \to K^+\rho^0(770))/$, $(D^+ \to K^-\pi^+\pi^+) < 0.0067$. The D_s^+ results are: , $(D_s^+ \to K^+\pi^-\pi^+)/$, $(D_s^+ \to \phi\pi^+) = 0.28 \pm 0.06 \pm 0.05$, , $(D_s^+ \to K^{*0}(892)\pi^+)/$, $(D_s^+ \to \phi\pi^+) = 0.18 \pm 0.05 \pm 0.04$, and , $(D_s^+ \to K^+\rho^0(770))/$, $(D_s^+ \to \phi\pi^+) < 0.08$.

To my parents, John and Martha Grim, and to Donna.

Acknowledgements

It is impossible to properly acknowledge everyone who has supported this work. Without question, the person who has been most supportive and with whom I am in the greatest debt, is my wife Donna. Without her endless sacrifice and unfailing love this work would not exist.

To bring an experiment like this from a concept to dissertation requires a leadership with vision, expertise, perseverance, and energy. Joel Butler, Jim Wiss, John Cumalat, and the rest of the E-687 leadership all possess seemingly endless amounts of these qualities and it is the direct result of their passionate pursuit of physics that this experiment has demonstrated itself to be the success that it is.

Of course, to accomplish what the leaders envision, an army of physicists and technicians must march on each problem. To all of the E-687 collaboration, I am deeply indebted. Among these scientists, there are a few individuals who have made this process a little more tolerable and some who deserve special recognition. I would like to thank Carlo Dallapiccola for his friendship, support and perspective.

I would also like to thank Luca Cinquini for the work and support he provided during the 10 months we worked on and supervised the "Pass1" reconstruction of our data. Will Johns and Brian O'Reilly deserve many kudos for their tireless efforts at ensuring the quality of the E-687 detector systems, and Ray Culbertson deserves special recognition for his efforts in writing the SDVERT software, which is the basis for most E-687 analyses. I would like to thank Phil Yager for the financial support provided and for opening his home to me during the many weeks of data collection and meetings in Illinois. Finally, I would like to single out John Cumalat for special recognition. As Carlo Dallapiccola has acknowledged, John's enthusiastic spirit is contagious and intoxicating. His willingness to discuss physics at any level and nurture the developing scientist is a luxury any experiment would be lucky to have.

Contents

List of Tables

List of Figures

Chapter 1

Introduction

This work concerns itself with study of the doubly Cabibbo suppressed decay $D^+ \to K^+\pi^-\pi^+$ and the singly Cabibbo suppressed decay $D_s^+ \to K^+\pi^-\pi^+$. Figure 1.1 shows the tree level quark diagrams for the decays $D^+ \to K^-\pi^+\pi^+$, and $D^+ \to K^+\pi^-\pi^+$. The tree level diagrams for $D_s^+ \to K^+K^-\pi^+$ and $D_s^+ \to K^+\pi^-\pi^+$ decays are shown in Figure 1.2. If the Cabibbo-Kobayashi-Maskawa model of quark mixing is assumed, then the decay rate for the upper diagrams of each figure will be proportional to $|V_{cs}V_{ud}^*|^2$, while the lower rates will be proportional to $|V_{cd}V_{ud}^*|^2$ and $|V_{cd}V_{us}^*|^2$ for the D^+ and D_s^+ respectively. It is a well established[1] that $|V_{cs}|^2 \simeq |V_{ud}|^2 \simeq 25 \times (|V_{cd}|^2 \simeq |V_{us}|^2)$. Hence, a decay amplitude which is proportional to $|V_{cs}V_{ud}^*|$ is considered to be favored while a diagram proportional to $|V_{cd}V_{ud}^*|$ or $|V_{cs}V_{us}^*|$ is considered to be singly suppressed, and a diagram proportional to $|V_{cd}V_{us}^*|$ is doubly suppressed. The study of quark-mixing doubly and

singly suppressed decays are interesting for several experimental and theoretical reasons.

Experimentally, there has been some controversy and ambiguity regarding previous doubly suppressed observations. The earliest attempt to search for the decay $D^+ \to K^+\pi^-\pi^+$ was performed by the Mark I collaboration[2]. The results of the search netted $0.0^{+4.7}_{-0.0}$ events and the upper limit at 90% confidence level

$$\frac{,(D^+ \to K^+\pi^-\pi^+)}{,(D^+ \to K^-\pi^+\pi^+)} \quad < \quad 5\% \tag{1.1}$$

was measured. As for other doubly suppressed charm decays, in 1992, Fermilab experiment E-691 published[3] an observation of the decay $D^+ \to \phi K^+$. The D^+ signal contained $4.5^{+2.4}_{-2.0}$ events which was used to measure the ratio of partial widths

$$\frac{,(D^+ \to \phi K^+)}{,(D^+ \to \phi\pi^+)} \quad = \quad (5.8^{+3.2}_{-2.6} \pm 0.7) \times 10^{-2}. \tag{1.2}$$

where the first set of error bars is statistical and the second is the systematic uncertainty of the experiment[1]. It is interesting to note that no effort was made to present evidence for the inclusive decay $D^+ \to K^+K^-K^+$. Subsequent to this paper, CERN experiment WA-82 published[4] a $D^+ \to K^+K^-\pi^+$ signal with 13.1 ± 4.5 events which was used to calculate the ratio of partial widths

$$\frac{,(D^+ \to K^+K^-K^+)}{,(D^+ \to \phi\pi^+)} \quad = \quad 0.49 \pm 0.23 \pm 0.06, \tag{1.3}$$

This inclusive rate is 10 times the rate of the E-691 ϕK^+ rate. Given this difference

[1] This convention will be adhered to throughout this work.

and the very poor quality of the signals, it is unclear whether the two analyses are inconsistent, and consequently how large the $D^+ \to K^+K^-K^+$ decay rate is.

More recently, the CLEO collaboration has published[5] a $D^0 \to K^+\pi^-$ signal with 19.1 ± 6.1 events. The CLEO II detector does not have good vertexing capabilities which means the lifetime of the candidate events could not be accurately measured. Thus, it is uncertain whether this signal could be due to $D^0 - \bar{D}^0$ mixing or doubly suppressed decays. Nonetheless, they calculate the ratio of partial widths

$$\frac{, (D^0 \to K^+\pi^-)}{, (D^0 \to K^-\pi^+)} = 0.0077 \pm 0.0025 \pm 0.0025. \tag{1.4}$$

In summary, in the nearly 21 years since the discovery of the charm quark, the least ambiguous and controversial measurement pertaining to doubly suppressed charm decays was the Mark I upper limit on the $D^+ \to K^+\pi^-\pi^+$ branching ratio. This measurement was made just 3 years after the discovery of the charm quark.

The history of the decay $D_s^+ \to K^+\pi^-\pi^+$ is slightly less controversial and ambiguous. In 1990, CERN experiment NA-32, the ACCMOR collaboration, performed a search for the decay mode $D_s^+ \to K^+\pi^-\pi^+$ and found 1.4 ± 1.8 events[6]. From this search, and a topological normalization of the data performed subsequently[7], the following branching fraction was calculated

$$\frac{, (D_s^+ \to K^+\pi^-\pi^+)}{, \, total} = 0.003^{+0.004}_{-0.003}. \tag{1.5}$$

Since doubly suppressed decays have yet to be unambiguously seen, they

provide the next level for testing the predictive power of current theoretical efforts. It is possible though to make naive predictions for the level at which these decays might occur. As was discussed earlier, the decay rate for the favored diagrams will be proportional to $|V_{cs}V_{ud}^*|^2$, while the singly and doubly suppressed rates will be proportional to $|V_{cd}V_{ud}^*|^2$ and $|V_{cd}V_{us}^*|^2$ respectively. Using the latest measurements of the weak mixing angles[1] and tree level amplitudes, the following ratios may be calculated

$$\frac{, (D^+ \to K^+\pi^-\pi^+)}{, (D^+ \to K^-\pi^+\pi^+)} \sim 0.003, \tag{1.6}$$

$$\frac{, (D_s^+ \to K^+\pi^-\pi^+)}{, (D_s^+ \to K^-K^+\pi^+)} \sim 0.054. \tag{1.7}$$

Beyond this level of prediction one must somehow incorporate the effects of the color field and the hadronization process. There have been many different theoretical approaches to understanding non-leptonic charm decays, *e.g.* the $1/N_c$ expansion of Buras, Gérard, and Rückl[8], the QCD Sum Rules approach of Blok and Shifman[9, 10, 11, 12], and Heavy Quark Effective Theory[13, 14, 15, 16, 17, 18]. All these approaches have difficulties which limit their ability to calculate accurately decay rates of charm hadrons[19]. To date, the most successful theoretical approach has been a phenomenological modeling of the weak decay process[20, 21, 22, 23, 24, 25, 26, 27]. This approach requires experimental data to tune input parameters. In order for these models to have continued success, they must continually be checked against new data as it becomes available, and the parameters readjusted in the

hopes that new insight may be gained. Only recently have the models evolved to the point where predictions for doubly suppressed decays of the D^+ meson have become possible [28, 29]. Chau and Cheng[28] predict the following D^+ branching fractions,

$$BF(D^+ \to K^+\rho^0) = 1.0 \times 10^{-4} \quad (1.8)$$

$$BF(D^+ \to K^{*0}\pi^+) = 1.1 \times 10^{-4} \quad (1.9)$$

$$BF(D^+ \to \phi K^+) = 0.5 \times 10^{-4} \quad (1.10)$$

Comparisons to the $K^+\rho^0$ and $K^{*0}\pi^+$ predictions are made in the summary.

There are several other interesting reason for studying suppressed decays. For example there exists the possibility for observing new physics. Significant deviations from the ratios shown in equation 1.6, could be signals for a new intermediate boson[19]. Other causes for deviations could be interference effects due to external and internal W emission diagrams shown in the figures. It is this mechanism which is believed to cause the narrower D^+ total width relative to the D^0 total width. The effect of this narrowing of the total width may cause in enhancement in the suppressed partial width, which would be interesting to observe. This must be mitigated by the fact that hadronization of the quarks must be considered during the weak decay process, and this process is not yet modeled accurately.

Regardless of the status of theoretical models or presumptions regarding decay mechanisms, detailed studies of fundamental particles and their interactions

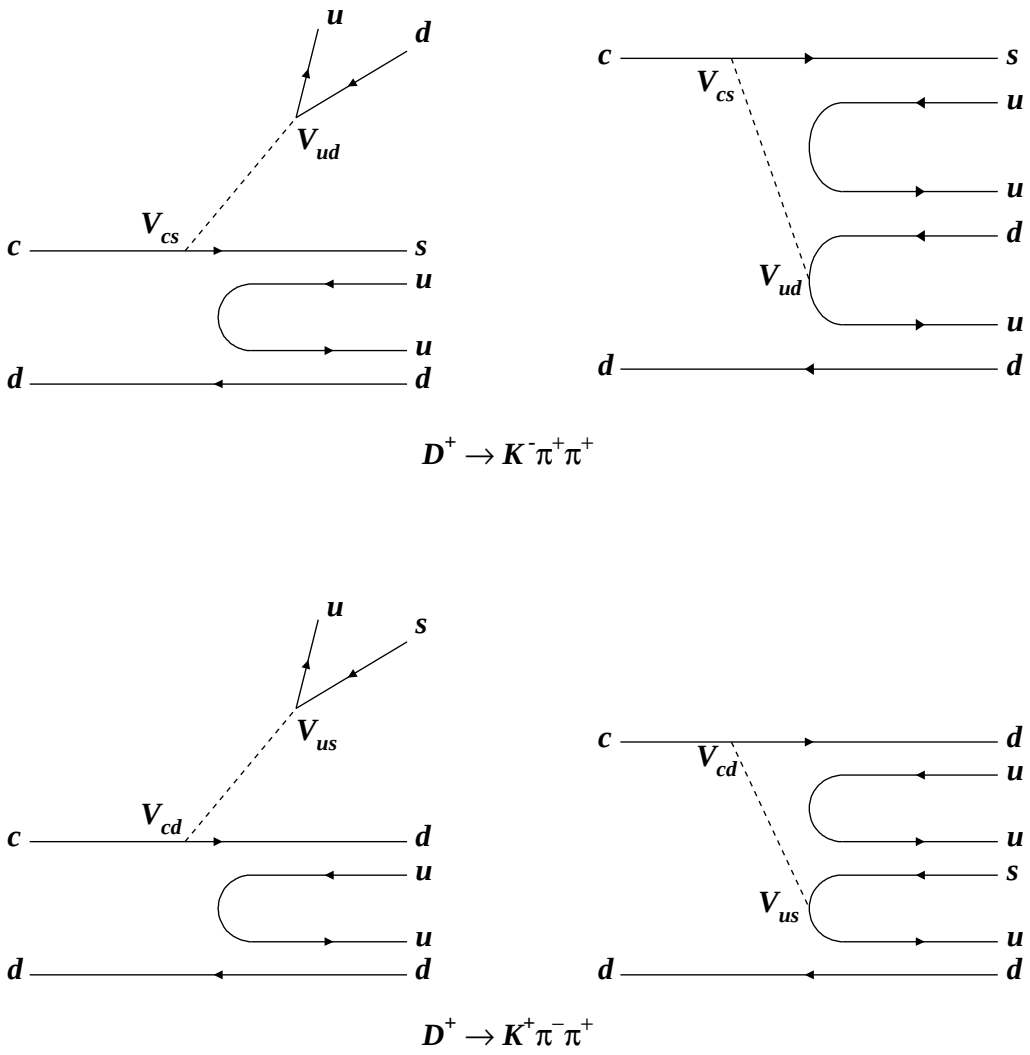

Figure 1.1: The quark diagrams for tree level $D^+ \to K^-\pi^+\pi^+$ and $K^+\pi^-\pi^+$ decays.

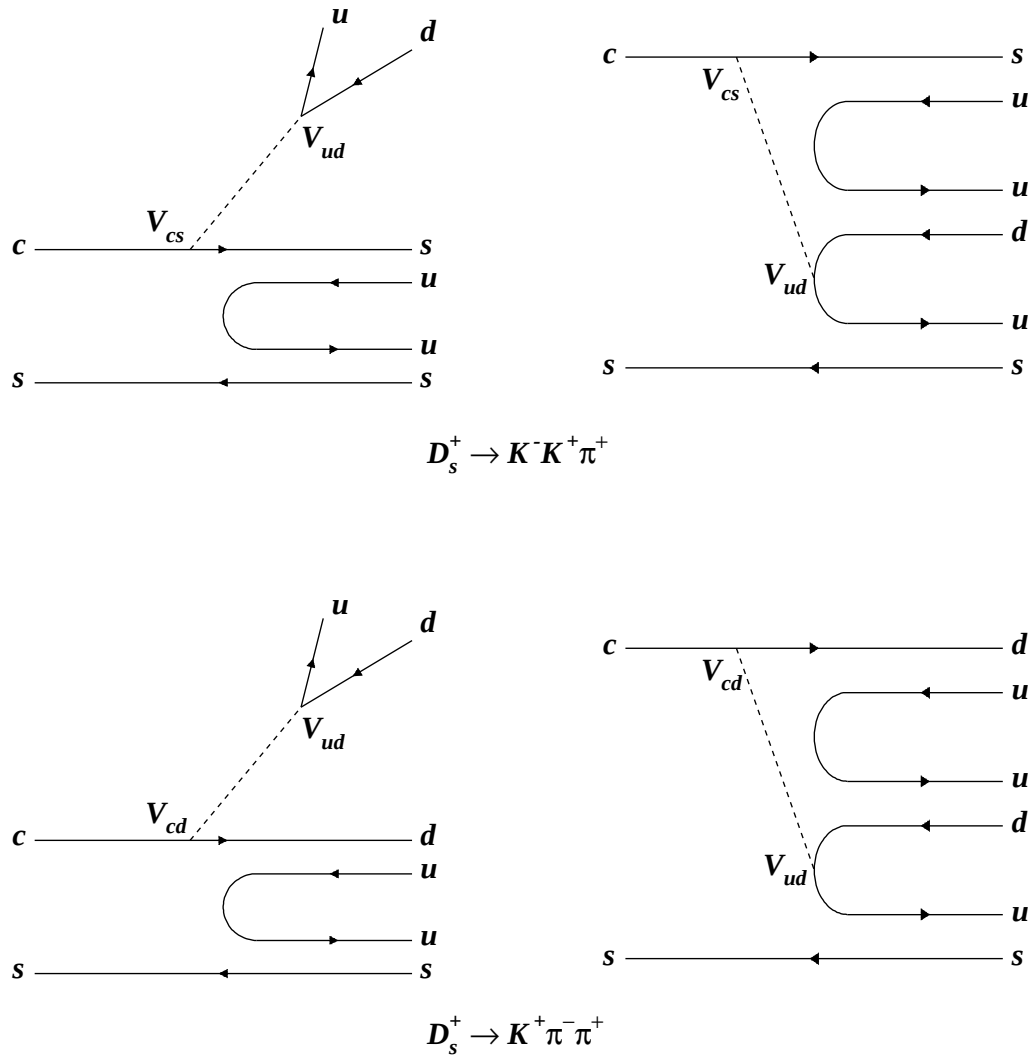

Figure 1.2: The quark diagrams for tree level $D_s^+ \to K^-K^+\pi^+$ and $K^+\pi^-\pi^+$ decays.

provide the truth required for all efforts to understand the universe. Broadening this knowledge base is fundamental and the motivation of all experimental science.

Chapter 2

Photon Beam Production

In Nuclear Physics, the generation of photons from tens of KeV to several MeV can be as "simple" as waiting for the appropriate reaction to occur and a little collimation. Unfortunately, to extend this energy range by factor of 1000, one must employ the use of charged particle accelerators and devise a scheme to distill the required precipitates. At Fermilab this process begins with the generation and acceleration of protons and ends with the highest energy photon source since the earliest moments of the Universe.

2.1 The Proton Beam

The beam of protons which make their final turn inside the Tevatron, have traversed some 4.5 million miles of vacuum and several different acceleration phases. The

genesis of this trek is the Cockroft-Walton accelerator, where electrons are added to hydrogen atoms. The resulting negative ions are subsequently accelerated to 750 kilovolts of kinetic energy using a potential difference. Following the Cockroft-Walton, the negative ions are sent to a linear accelerator (LINAC) where they are further boosted to 400 MeV in 175 meters of drift tubes spaced at increasing lengths of separation. Upon exiting the LINAC, the H^- ions are stripped of electrons by a carbon foil before entering the third stage of acceleration, now as protons.

At this point, roughly a factor of 10^7 has been gained in energy in just over 175 meters. Unfortunately, to gain another factor of 10 would require a LINAC that approached 2 kilometers. This would be unwieldy as an injector for the Main Ring. Consequently, the 400 MeV protons are supplied to the subterranean, 500 foot diameter, Booster Ring. Here the protons are brought to 8 GeV of energy in just over 33 milliseconds. The Booster normally cycles twelve times in rapid succession, loading twelve bunches of protons into the Main Ring, the next stage of the acceleration process. The Main Ring resides 20 feet below ground level in a 6.28 km circumference tunnel. The tunnel is 10 feet in diameter and houses 1000 conventional copper-coiled magnets which focus and direct the beam during its acceleration to 150 GeV. Finally, the very relativistic protons are handed off to the Tevatron which resides in the same 6.28 km tunnel. The Tevatron's super-conducting magnets lie directly below the Main Ring magnets, but operate at liquid helium temperatures of 4K, roughly 290K below the temperature of the Main Ring

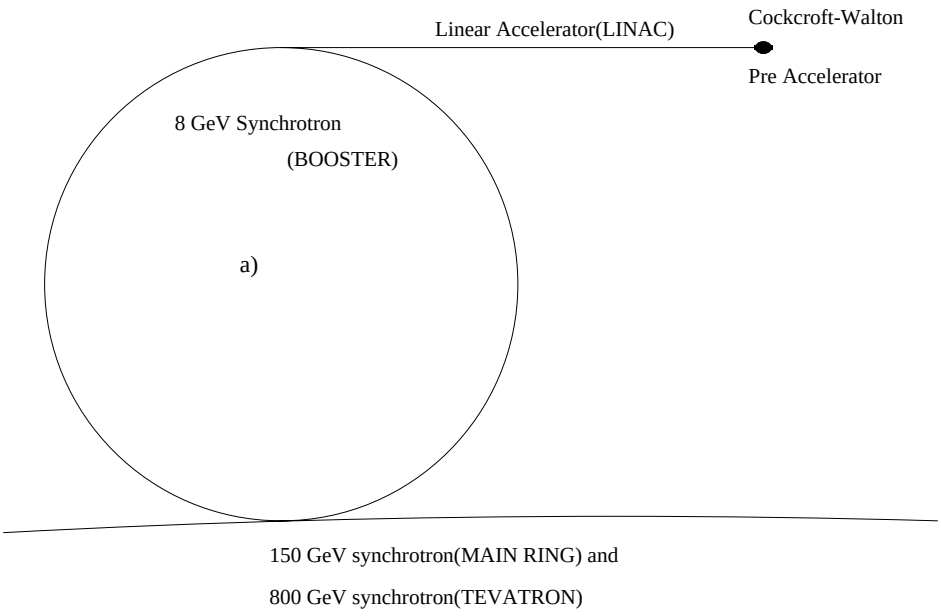

Figure 2.1: Fermilab's 800 GeV/c Proton Accelerator.

magnets. During the final acceleration stage, the proton bunches totaling 10^{13} protons, are brought to 800 GeV of energy, currently the worlds highest energy particle beam. This process is summarized in Figure 2.1. The accelerated proton beam can then be used for collisions, or it can be provided to the fixed target area to supply the many beam line available. The extraction of the proton beam is shown in Figure 2.2.

Figure 2.2: Proton extraction into the Fermilab Fixed Target Areas.

2.2 The Photon Beam

To create photons, an elaborate conversion and cleansing process is required. Issues of intensity and purity are driving concerns behind the decisions regarding materials and acceptance cuts used to provide such a high energy gamma source. The photon beam is produced by first sending the 800 GeV/c protons into a primary production target. This target was usually liquid deuterium. The resulting charged particles were swept into a charged particle dump while the neutral beam, primarily comprised of neutrons, K^0's, Λ^0's, and photons from π^0 decays, was allowed to continue through a small hole in the dump. The neutral beam then struck a lead converter of 50% of a radiation length. Roughly half the photons from the π^0 decays were converted to e^+e^- pairs, whereas hadronic neutrals were unlikely to interact and continued forward into a neutral dump. Subsequent to the lead converter, a charged particle transport system split the e^+e^- pairs and swept them around the neutral dump. During the 1990-91 Fixed Target running, the positron arm was blocked off and only the electrons were transported. The transport optics were tuned to select a momentum bite of 350 ± 45 GeV/c, This large momentum bite was required to improve beam flux. After the momentum selection, the electrons passed through a beam tagging system of silicon microstrip detectors and magnets. The electron flux was then directed to a lead radiator which produced high energy photons via bremsstrahlung. This process is summarized in Figure 2.3 while the

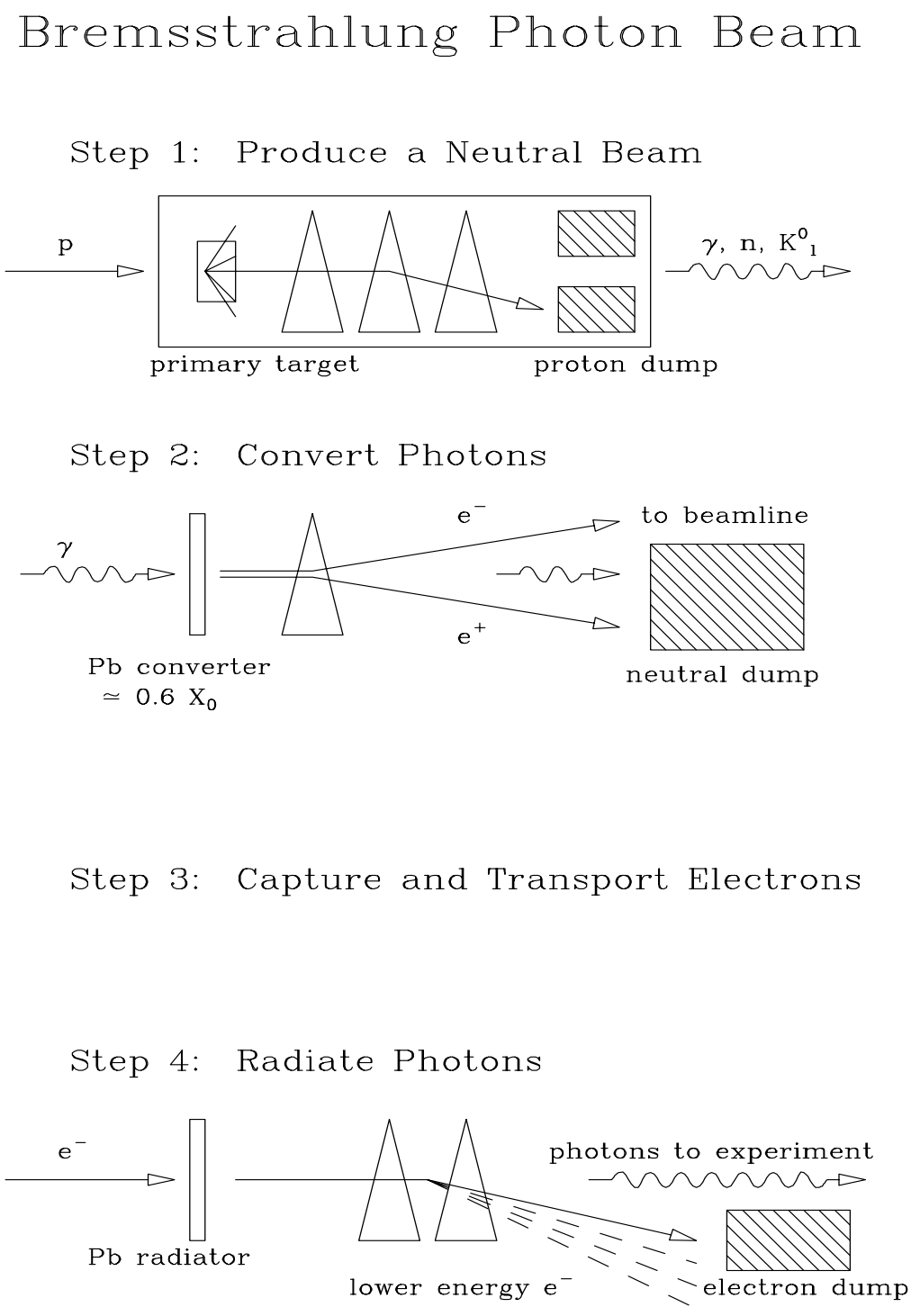

Figure 2.3: Photon beam production summary.

Figure 2.4: Momentum spectrum of all photons produced by the radiator.

beam line characteristics are summarized in Table 2.1. The momentum spectrum of all photons radiated is shown in Figure 2.4. As can be seen, the experimental beam striking the target covers a "wide band" of momentum.

Table 2.1: Beam line properties.

Beam Element or Characteristic	Property	Value
Primary Target		
	Material	Liquid D_2
	Physical Length	3.5 m
	Interaction Length	1.0
Photon Converter		
	Material	Pb
	Radiation Length	$\sim 50\%$
Electron Radiator		
	Materials	Pb, Si and other
	Radiation Lengths	20% Pb, 1.6% Si, $\sim 3\%$ other
Beam Size at Production Target		
	Horizontal	$\delta x = \pm 1$ mm
	Vertical	$\delta y = \pm 1$ mm
Beam Acceptance		
	Horizontal	$\delta\theta_x = \pm 1.0$ mrad
	Vertical	$\delta\theta_y = \pm 0.75$ mrad
	Momentum Bite	$\Delta p/p \approx \pm 15\%$
Photon Beam Size at Experimental Target		
	Horizontal	$\delta x = \pm 1.25$ cm
	Vertical	$\delta y = \pm 0.75$ cm
Photon Beam Divergence at Experimental Target		
	Horizontal	$\delta\theta_x = \pm 0.6$ mrad
	Vertical	$\delta\theta_y = \pm 0.5$ mrad

Chapter 3

The E-687 Spectrometer

The apparatus used in experiment 687 resides in the Wide Band Photon Lab at the end of the Proton beam line at Fermilab. Figure 3.1 gives an overview of the equipment used and referred to in this and subsequent chapters. The photon beam, described previously, is brought into the hall where it strikes the experimental target. The dominant interaction in the target is e^+e^- production, but of all hadronic interactions, approximately 1% contain charm. In p+N and π+N interactions, the charm production rates are ten times smaller[30, 31]. It is the relatively large charm production cross section of the $\gamma + N$ interaction that motivates the beam choice and the decisions regarding the experimental target, trigger and particle detectors.

Subsequent to a photon-nucleon interaction, many particles will be produced and traverse the E-687 spectrometer. The spectrometer has been optimized for the

acceptance of decays of high mass ($\sim$ few GeV/c^2) particles with a broad momentum spread (1-200 GeV/c^2). Since γ+N interactions often produce tens of particles, the ability to track and record this independent information simultaneously was required. To facilitate this, the spectrometer was divided into 2 geometric acceptance regions, the inner region covering $|\theta_x| < 30$ mr and $|\theta_y| < 50$ mr and the outer region covering out to angles $|\theta_x| < 100$ mr and $|\theta_y| < 150$ mr. These acceptance regions are covered by detectors designed to track, momentum measure, and identify charged particles. The spectrometer also includes capabilities for measuring electromagnetic and hadronic energy and the identification of muons. The following chapter describes the elements that comprise this spectrometer with emphasis on the systems used in the analysis included in this work.

3.1 Coordinate Systems

Experiment 687 (E-687) uses two separate right handed coordinate systems within the spectrometer for specifying momentum and vertex information. The z-axis of both systems coincide and are aligned with the photon beam direction, while the origins are offset. The M2 coordinate system has its origin located at the center of the M2 analysis magnet, with the y direction defined vertically and away from the earth. The Granite Block coordinate system has its origin at the edge of the granite block supporting the microstrip tracking system and its y direction defined as in the

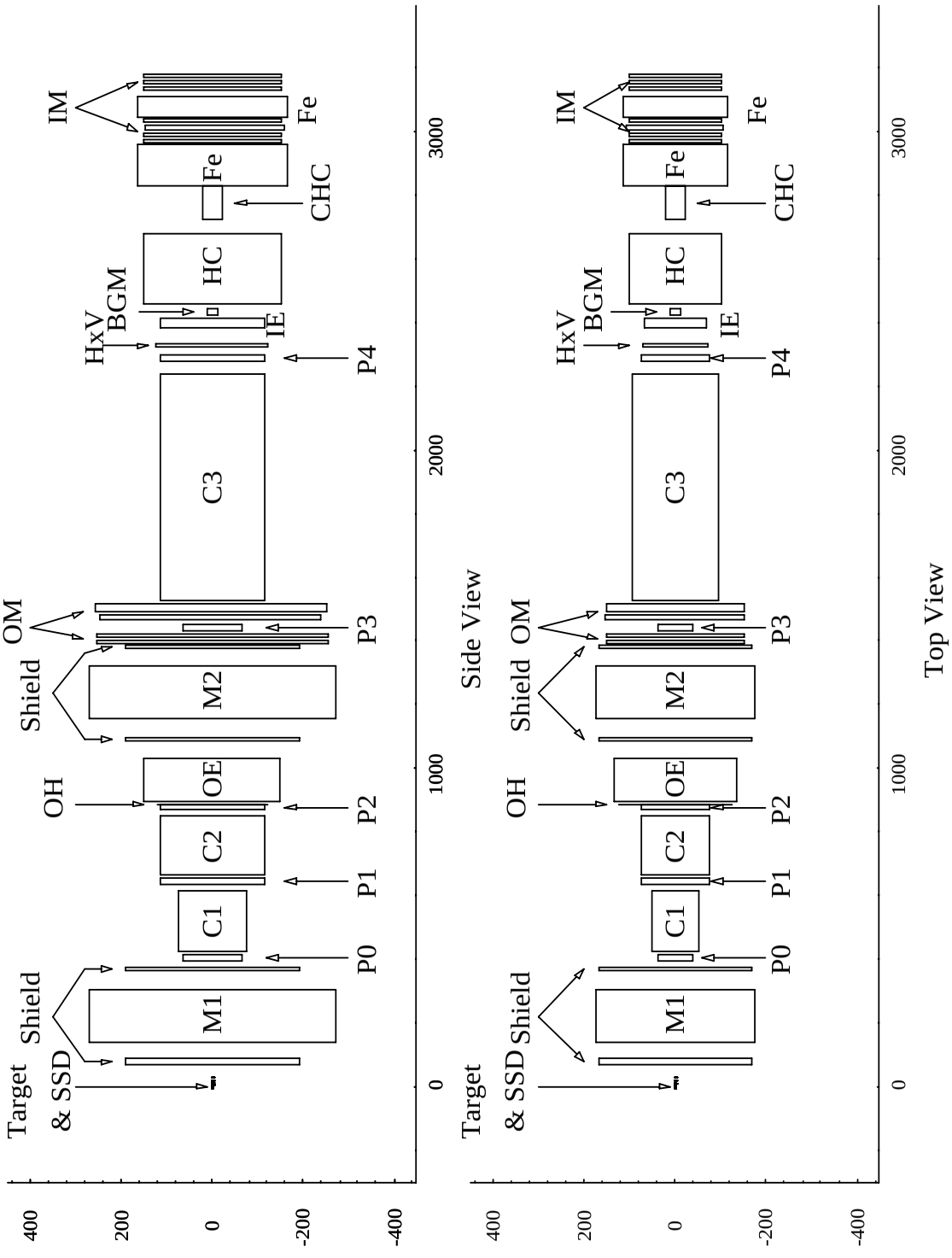

Figure 3.1: The E-687 Spectrometer.

M2 system. The offset between the two coordinate systems is approximately 1240 cm.

3.2 The Target

Since E-687 uses a photon beam, the dominate source of particles which pass through the spectrometer are those resulting from pair production in the target. Since the primary research goal of E687 is to study interactions of a hadronic nature, the optimal choice for a target is a material which contains the largest ratio of radiation length to interaction lengths as possible. Another concern for target material is the size. The target needs to be large enough to produce a significant number of interesting events while compact enough to reduce the amount multiple Coulomb scattering and provide adequate acceptance for the charm decay products.

E-687 used a Beryllium target for the vast majority of runs. Beryllium has a ratio of radiation to interaction length 0.85[1] and is relatively inexpensive. For $\sim 37\%$ of the data taking, a 9 segment target was used. Each segment was 2.54cm $\times$ 2.54cm $\times$ 4mm, and the target was created by packing all segment together. This gave an overall length of 3.6cm or 10.1% of a radiation length. The majority of the remaining data was taken with an 11 segment target using the same segment dimensions. This corresponds to a 4.4cm target, or 12.4% of a radiation length.

Figure 3.2: The microstrip detector layout.

3.3 Charged Particle Tracking

3.3.1 The Microstrip Detector

Table 3.1: Microstrip Detector Properties

Property	Station 1	Station 2	Station 3	Station 4
Active Area (cm^2)	2.5×3.5	5×5	5×5	5×5
High Res. Area (cm^2)	1.0×3.5	2×5	2×5	2×5
Strip Pitch (μm)	25,50	50,100	50,100	50,100
No. of Channels	688×3	688×3	688×3	688×3

Tracking in the region after the target and before the first analysis magnet was performed by several planes of silicon microstrips shown schematically in Figure 3.2. Table 3.1 lists the various properties of the system. The system was designed to perform the very high precision tracking required to reconstruct charm decay vertices. The detector consisted of 12 planes of silicon microstrips grouped in 4 stations, mounted on a granite block support. The granite block provides an alignment accuracy of $\pm 3\mu$m over 5 cm. Each station contained 3 planes, measuring the i, j and k coordinates, respectively, of charged tracks. The i, j, k coordinates are defined relative to the x axis by rotations of -135^o, -45^o, and -90^o. The innermost region of the upstream station contains a segmentation which is twice that of the rest of the system. This provides the highest resolution possible for the most energetic tracks. Each strip is read out into one of 8,256 ADC channels required for the entire detector system.

3.3.2 The Analysis Magnets

After the microstrip tracking system, charged particles were deflected in the first of two momentum analysis magnets. The two magnets, referred to as M1 and M2, were identical in design, but operated at different field strengths. The magnets were oriented to deflect charged particles vertically and in opposite directions. They each have a maximum p_t kick of 1 GeV/c and were operated at 0.40 and 0.85 GeV/c respectively. The ratio of these kicks was arranged to return charged tracks to their undeflected position toward the downstream end of the spectrometer, near the Inner Electromagnetic calorimeter. This arrangement aids in the rejection of the electromagnetic background as the e^+e^- pairs are produced with very little p_t and are more or less returned to the beam profile downstream. Effects of bremsstrahlung smear the profile some. Hadronic events are generally produced with a nominal amount of p_t and typically have several tracks outside the pair region. By placing a trigger counter, the H$\times$V hodoscope for example, at the position at which the pair profile reconstitutes and requiring hits outside this region, the rejection of this background can be greatly enhanced. Table 3.2 lists the physical characteristics and operating properties of the analysis magnets.

Table 3.2: Analysis Magnet Properties

Central Field	14.0 kilogauss
Maximum p_t kick	0.97 GeV/c
Field Uniformity	$\pm 2.5\%$
Steel yoke length	66 in.
Effective length	101 in.
Total length	104 in.
Maximum Current	2500 amps
Voltage at max. current	160 Volts
Total flow (50% glycol)	118 gpm
Pressure drop across coils	150 psi
Conductor Diameter	1.855 in. x 1.375 in.
Water passage diameter	0.61 in.
Total Weight	272 tons

3.3.3 The Multiwire Proportional Counter System

Five stations of Multiwire Proportional Counters (MWPC) were used for tracking charged particles downstream of the first analysis Magnet. The chambers are referred to as, P0, P1, P2, P3, and P4. They occupy the positions shown in Figure 3.1. With chambers P0-P2 located between M1 and M2 and chambers P3 and P4 downstream of M2, two separate momentum measurements are possible for a track traversing at least the first 4 chambers. Wide angle tracks unable to meet the acceptance requirements of M2 may still have the M1 momentum measurement.

There were 2 types of detectors used, Type I (P0 and P3) and Type II (P1, P2 and P4). Type I detectors were smaller than the Type II detectors due to the

Table 3.3: Multiwire Proportional Counter Properties

Property	Type I	Type II
Aperture (in^2)	30×50	60×90
Wire Spacing (mm)	2.0	3.0 (3.3 for P4)
Anode Wire Thickness (μm)	20	25
Cathode Wire Thickness (μm)	64	89
Equivalent Tension (grams)	65	90
No. X-view Wires	376	512
No. Y-view Wires	640	768
No. U/V-view Wires	640	832

shadowing of the magnet yokes. Type I stations matched the aperture of the magnets they followed which was 30 in. $\times$ 50 in. ($x \times y$) and the Type II had dimensions of 60 in. $\times$ 90 in. Each station contained 4 planes of wires, measuring the Y, V, U, and X positions of each track. The X view wires ran vertically, while the Y view ran horizontally. The stereo views V and U had wires running $\pm 11.3^{o}$ with respect to horizontal. Table 3.3 summarizes the properties of the MWPC system.

3.4 Particle Identification

3.4.1 The Čerenkov Detectors

E-687 used three threshold Čerenkov counters to identify charged particles. The counters were flushed with different gases at slightly above atmospheric pressure. The gasses were chosen to optimize the identification of heavy particles such as

Table 3.4: Čerenkov Counter Properties

Counter	No. of Cells	Gas	Threshold (GeV/c)		
			pion	kaon	proton
C1	90	80% He, 20% N_2	6.6	23.3	44.3
C2	110	N_2O	4.5	16.2	30.9
C3	100	He	17.0	61.0	116.2

kaons. For the 3 counters used, Table 3.4 lists the operating parameters of each of the detectors. The identification scheme used by these detectors is base on the principle that a charged particle will radiate Čerenkov light when it is above the threshold momentum,

$$P_{thresh} = \frac{mc}{\sqrt{2(n-1)+(n-1)^2}}, \tag{3.1}$$

where n is the index of refraction of the medium, m is particle mass and c is the speed of light. This creates unique light patterns among the 3 counters for different particles of the same momentum. This can be exploited for identification purposes as will be discussed further in the next chapter. Table 3.5 summarizes these identification capabilities.

The C1 Detector

The first Čerenkov detector was located between P0 and P1, approximately 5m downstream of the target. C1 used a He/N_2 (80%/20%) gas mixture. The active transverse area of the detector was 50 in. $\times$ 80 in. with a total length of 71 in.

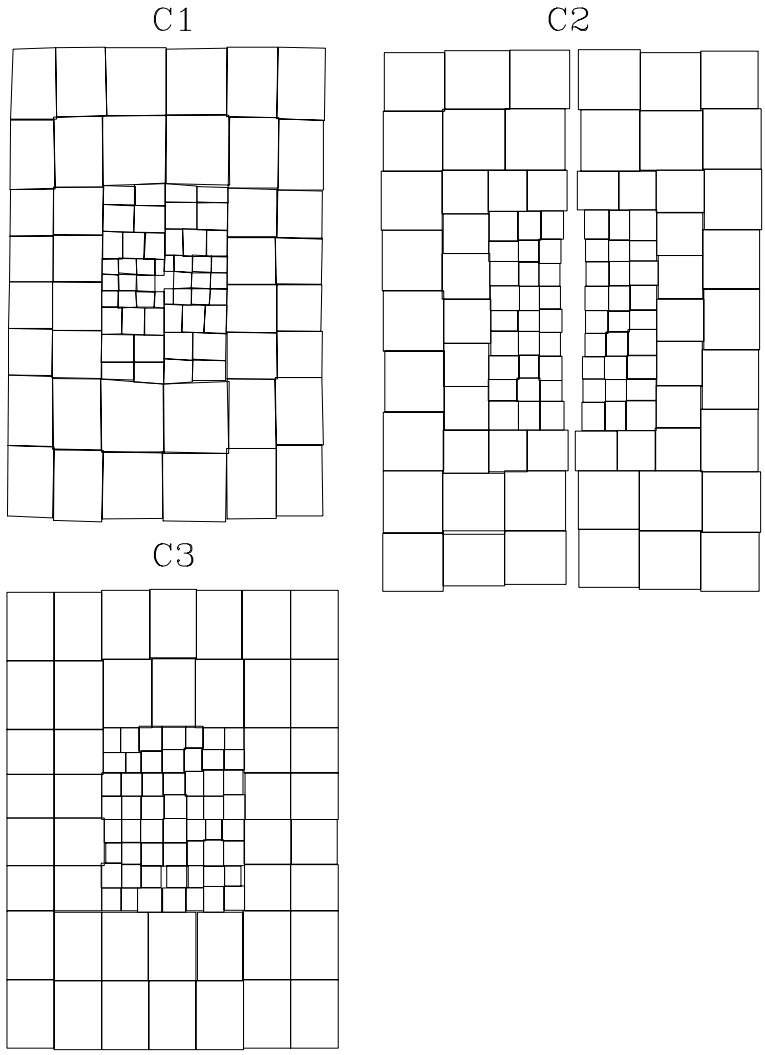

Figure 3.3: Cell Geometry for E-687 Čerenkov Counters.

Table 3.5: Particle Identification Regions

Particle	5-chamber track (GeV/c)	3-chamber track (GeV/c)
$e^{\pm}$	$0.16 - 17.2$	$0.16 - 6.6$
$\pi^{\pm}$	$4.9 - 17.2$	$4.9 - 6.6$
$e^{\pm}$ or $\pi^{\pm}$	$17.2 - 60.8$	$6.6 - 23.3$
$K^{\pm}$	$17.2 - 44.3$	$17.2 - 23.3$
p	$17.2 - 44.3$ and $65.7 - 115.5$	$17.2 - 44.3$
$K^{\pm}$ or p	$4.9 - 17.2$	$4.9 - 17.2$

The detector was constructed using conventional and planar focusing[32] mirrors for a total of 90 cells. The cell geometry is shown in Figure 3.3. For a singly charged particle traveling at $\beta = 1$ and having the forward Čerenkov cone completely spanned by a Čerenkov detector cell, the number of photoelectrons produced by the cell is a measure of the performance of the detector. The cells in the planar section of the detector provide 3.6 photoelectrons for a $\beta = 1$ particle while the cells in the conventional section provide 2.5 photoelectrons.

The C2 Detector

The second Čerenkov detector was located between P1 and P2, approximately 7.5m downstream of the target. C2 used a N_2O gas mixture. The active transverse area of the detector was 64 in. $\times$ 94 in. with a total length of 74 in. The detector was constructed with a total of 110 cells. The cell geometry is also shown in Figure 3.3. The gap in the central region of the cell structure was designed to reduce material

in the pair region of the spectrometer. The C2 cells provide 10.0 photoelectrons for a $\beta = 1$ particle.

The C3 Detector

The third Čerenkov detector was located between P3 and P4, approximately 15m downstream of the target. C3 used He gas. The active transverse area of the detector was 60 in. $\times$ 93.25 in. with a total length of 277 in. The detector was constructed using 100 spherical glass focusing mirrors. The cell geometry is also shown in Figure 3.3. The C3 cells provide an average of 9 photoelectrons for a $\beta = 1$ particle.

3.4.2 The Muon System

The muon identification system is separated into inner and outer acceptance regions as described in the opening paragraphs of this chapter and are referred to as the IM and OM counters respectively. Both systems are comprised of iron filters, scintillator hodoscopes and proportional tube counters and are positioned as shown in Figure 3.1. The scintillating counters were used for triggering while the proportional tubes were used for track matching.

The proportional counter arrays were constructed from packages of 8 tubes ganged together. Each tube was constructed from of 5.08 cm diameter aluminum tubes with a 0.16 cm wall thickness. The gas used in the proportional tubes was Ar-CO_2 (80%/20%) and the tubes were operated ~ -2.6 kV, approximately 200 V

above the onset of the efficiency plateau.

The Inner Muon Detector

The IM detector covers an acceptance of roughly 0 to ± 40 mr in x and 0 to ± 60 mr in y. The detector is located at the downstream end of the spectrometer behind 121 cm of Fe, used as a filter. This filter is approximately 10 interaction lengths of material. The first part of the detector is comprised of an array of proportional tubes in 4 planes measuring x and y views, followed by a scintillating hodoscope split into 2 planes one horizontal and one vertical. The array covers an area of 2.0 m $\times$ 3.0 m. Just behind this hodoscope is another 60 cm of Fe which acts as a second filter. Behind the second filter resides another array of proportional tubes measuring x and y and one plane of horizontal scintillator. The were a total of 61 scintillator paddles and 320 proportional tube channels in the IM.

The Outer Muon Detector

The OM detector covers the acceptance region roughly ± 35 mr to ± 125 mr in x and ± 50 mr to ± 200 mr in y. The system is located just downstream of M2 and uses the magnet iron as a filter. The detector is comprised of 2 planes of proportional counters measuring x and y respectively, followed by a plane of horizontal and a plane of vertical scintillating paddles. The total area covered by the hodoscope was 3.0 m $\times$ 5.0 m. There were 89 scintillator paddles and 336 proportional tubes used

in the OM.

3.5 Calorimetry

E-687 had the capability of measuring both Electromagnetic and Hadronic energy passing through the spectrometer. Since a photon beam was used, the presence of hadronic energy was part of the trigger requirement. This was the primary use of the Hadron Calorimeter (HC) and Central Hadron Calorimeter (CHC). Since a number of hadrons have large branching ratios to final states containing electrons or photons, the Inner and Outer Electromagnetic Calorimeters (IE and OE) were also used in reconstructing these states offline. The Beam Gamma Monitor (BGM) and Beam Calorimeter (BC) were used to monitor beam flux and will not be discussed in this work.

3.5.1 Hadron Calorimetry

The Hadron calorimetry covered two geometric acceptance regions. The inner region, 0 mr to ± 5 mr, was covered by the CHC while the region from ± 5 mr to ± 30 mr was covered by the HC. The experimental trigger relied heavily on these two systems by requiring a minimum energy deposition between the two systems. The energy sum was required to be at least 40 GeV for the first 37% of the run and was increased to 50 GeV for the remainder. Since most hadronic events of interest

are produced with a p_t which falls outside the acceptance of the CHC, the task of triggering the experiment falls most heavily on the HC.

The HC

The HC is a steel, gas sampling calorimeter with tower readout geometry. The face of the HC covers an area of 203 $\times$ 305 cm^2 (x v. y), with a hole in the center of radius 15 cm. There are 28 steel plates sandwiching 28 sense planes which are immersed in an Argon-Ethane (50%/50%) bath. The sense planes are arrays of pads which detect the ionization from showering particles produced in the steel. Figure 3.4 shows geometry of the HC layout.

The CHC

The CHC is a uranium-scintillator calorimeter constructed of 16 layers of 16 in. $\times$ 16 in. $\times$ 1.5 in. depleted uranium slabs. The uranium slabs are interleaved with 1/4 in. polystyrene scintillator and readout by photomultipliers.

3.5.2 Electromagnetic Calorimetry

E-687 used two separate systems to reconstruct showers caused by photons from π^0 decays and electrons. The two systems covered the inner and outer acceptance regions and are referred to as the Inner Electromagnetic Calorimeter (IE) and the Outer Electromagnetic Calorimeter (OE).

Figure 3.4: The HC layout geometry.

The IE

The IE was located approximately 12m downstream of the target and had an active transverse area of 54 in. $\times$ 90 in. The detector was constructed from 100 sheets of 0.55 mil Pb, interleaved with sheets of 750 micron diameter scintillating fiber, giving an overall length of 30cm, or 25 radiation lengths. The fiber sheets alternated between x and y views, with 2 tiebreaking modules, of 3/8 in. $\times$ 2 in. scintillator, oriented at 45^o to resolve ambiguities. The detector was segmented longitudinally into 3 shower sampling regions, front, middle and back. The electron shower reconstruction efficiency was better than 80%.

The OE

The OE calorimeter was located 9m downstream of the target. The transverse area of the calorimeter was 255cm $\times$ 205cm, which contained a 51cm $\times$ 88cm aperture centered on the beam line. The detector was separated by a 9cm gap along the y axis to avoid the flux due to e^+e^- pairs. The overall acceptance of the OE was 28mr $\leq |\theta_x| \leq$ 142mr and 49mr $\leq |\theta_y| \leq$ 114mr. The calorimeter was constructed from 5 modules of alternating Pb, Al and plastic scintillator. The overall detector length was 18.4 radiation lengths.

Chapter 4

Data Acquisition and Reconstruction

The chapter describes the recording and reconstructing of an E-687 event. The emphasis of the chapter is on the detectors and logic used to trigger a hadronic event and the process of reconstructing physics observables pertinent to the analyses described later.

4.1 The Experimental Trigger

During the 1990-91 Fixed Target run at Fermilab, the Proton Beam line routinely transported 10^{12} protons per spill into the primary D_2 production target. This provided an average rate of electrons impinging the Pb radiator of approximately

20MHz, which produced a pair rate of about 2MHz in the spectrometer. Since the ratio of γp to pp cross sections is approximately 100 μb : 40 mb, the average hadronic rate in E-687 was on order of a few kHz. In order to reject the formidable pair rate presented by the photon beam, a two level trigger system was employed.

4.1.1 The Master Gate

The purpose of the Master Gate was to ensure a photon interacted in the target and produced at least two particles outside the nominal pair region. It is this topology which typically characterizes a hadronic event. Figure 4.1 shows the upstream elements used in the Master Gate. The counters A0 and A1 were used as vetoes to reject interactions caused by charged particles embedded in the beam. TM1 and TM2 were halo counters to reject charged particles, primarily muons, missing the veto counters. The trigger counters, TR1 and TR2, record the presence of charged particles downstream of the target and were required to fire in coincidence. Further, the Master Gate required at least 2 particles to be present in the downstream trigger hodoscopes, H$\times$V and OH, located as depicted in Figure 3.1. During the 1991 running, a scintillating tile hodoscope V$'$ was added into the master gate along with extra shielding in the pair region in front of the IE. V$'$ was located directly behind the IE and was useful in significantly reducing the amount of dead time. Figure 4.2 shows the layout of the H$\times$V, OH, and V$'$ scintillator tiles. To complete the first level trigger requirement, at least 2 hits were required to occur in the H$\times$V,V$'$

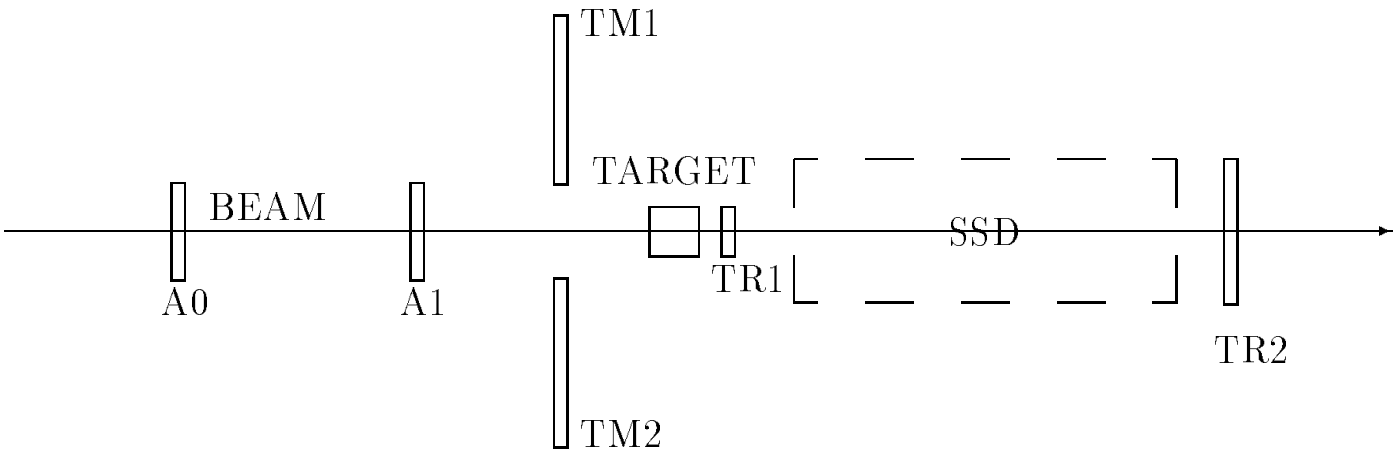

Figure 4.1: Trigger Counter Layout in the Target Region.

hodoscope, referred to as $(H \times V)_{2body}$, or one hit in H×V,V′, denoted $(H \times V)_{1body}$, and one hit in the OH. Using the detector names, the Master Gate trigger logic for approximately 70% of the run was given by,

$$MG = TR1 \cdot TR2 \cdot [(H \times V)_{2body} + (OH \cdot (H \times V)_{1body})] \cdot (\overline{A0 + A1}). \quad (4.1)$$

The remaining 30% of the running simply used $\overline{(A0 \cdot A1)}$ as the veto.

With this logic, the trigger rate for hadronic events was greater than 90%. The rejection efficiency for electromagnetic events was also greater than 90%, but the overall rate still remained in the tens of kHz; unacceptably high for recording hadron physics. Due to the nature of the counters used in the Master Gate, the first level trigger contributes a negligible amount of dead time. Once Master Gate

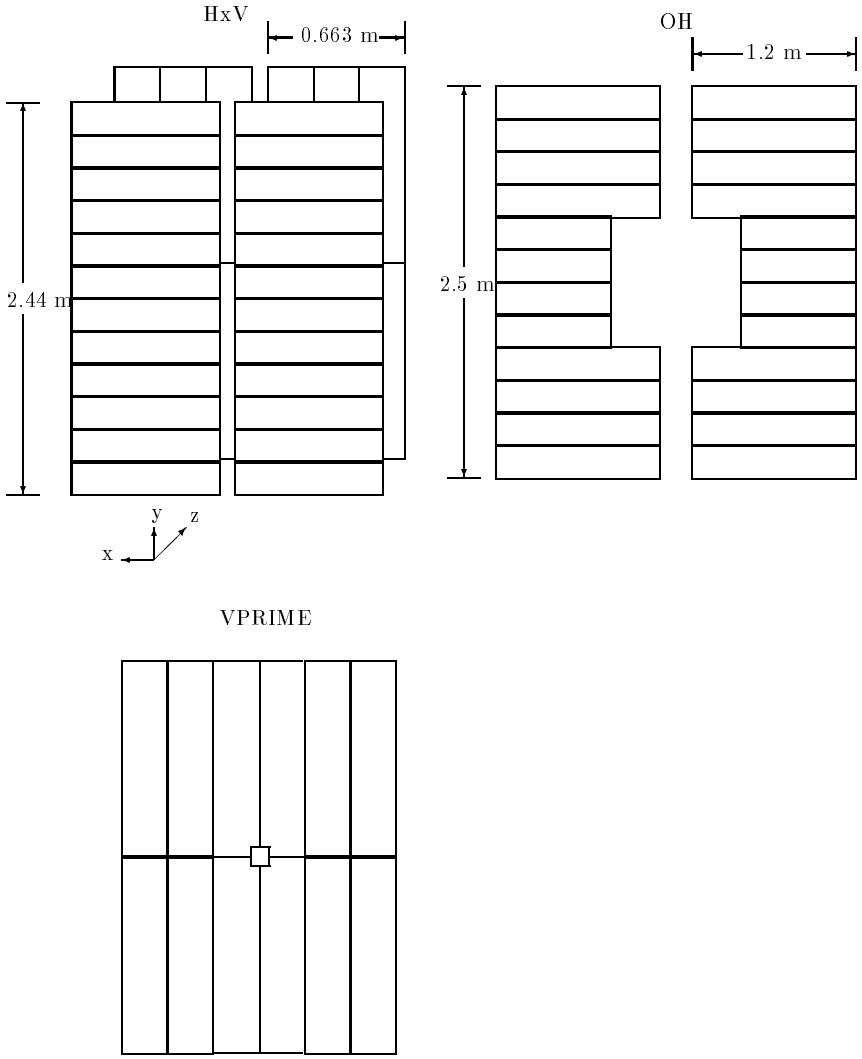

Figure 4.2: Scintillator configuration of the downstream trigger counters.

conditions have been met, gates were sent to the various readout systems. This caused all signals used in the second level trigger to be latched.

4.1.2 The Second Level Trigger

The second level trigger operates on latched signals and pulse heights from the various detector systems when a Master Gate occurs. These signals were processed by a series of specially designed trigger logic modules and ADC's. These logic modules form partial triggers called buslines, which were used as inputs to programmable trigger logic modules housed in a CAMAC crate. Each module comprises one trigger and can be programmed to require any of the 32 available buslines to be true or false. The output of each of these modules, is called a trigger, and the OR of all triggers in the crate constitutes the second level trigger. If no trigger has been received within 1.2 μs of the Master Gate, a clear cycle is executed. This clear cycle takes approximately 1.0μs. Thus, the total dead time for a Master Gate which fails to produce a second level trigger is approximately 2.2μs. If a second level trigger is generated, then a full readout and automatic clear is initiated.

For most of the normal running conditions encountered in E-687, the detector system requirements to issue a second level trigger were:

- At least three wire chamber hits in P0 outside the pair region.
- Energy deposited in the HC and CHC (when applicable) greater than 40 GeV

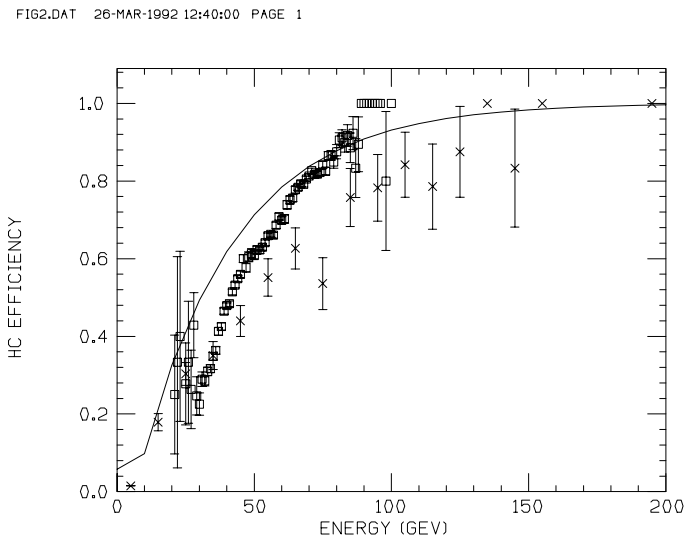

Figure 4.3: HC Trigger efficiency as a function of energy.

for the first 1/3 of the run and 50 GeV for the rest.

Figure 4.3 shows the efficiency for the HC busline as a function of incident energy as determined during calibration runs. Other triggers used during data collection included a pre-scaled Master Gate for offline trigger studies, a pre-scaled T1 trigger for unbiased sample studies and a μ pair trigger which looked for pairs of hits in the inner and outer muon hodoscopes.

4.2 Data Acquisition

After the Master Gate and second level trigger requirements, the Data Acquisition (DAQ) system is signaled to begin processing the many streams of data which must

be combined into an event and recorded on tape. There are five primary data streams which are readout out from the various detector systems; the ADC's, TDC's, Smart Crate Controller latches, and two Fastbus crate ADC's. The digitized information is read into Lecroy 1892 Fastbus memories before being combined into an event and queued into the event pool for buffering purposes. When ready, the event is written to one of 4 possible tape drives being used in parallel. During the 1990-1991 Fixed Target Run, E-687 wrote $\sim$ 510 million triggered events to tape. This data set required 1000 8mm data cassettes for storage, which corresponds to about 2.0 Terabytes of data.

4.3 Data Reconstruction

With a raw data set spanning 1000 8mm cassettes and 2.0 Terabytes, it is not feasible from a computing and storage standpoint to directly analyze the digitized information for physics. Thus, the entire data set was passed through an initial reconstruction phase, referred to as Pass1, where the digitized information was used to reconstruct particle tracks, momentum, vertices and particle identification. All successfully reconstructed events were then written to tape along with the original raw information. The output of this Pass1 phase was then passed through a Skim phase, where the reconstructed information of events satisfying at least one of the physics filters was written to tape. It took about a year and several thousand tape

mounts for this process to be completed, with the final result being a manageable data set which easily fits on a bookshelf.

4.3.1 The Pass1

An average raw event collected with the E-687 spectrometer takes about 15 seconds to reconstruct on a VAX-780 computer. With better than 500 million event written to tape, it would take this CPU several hundred years to completely reconstruct the full E-687 data set. During the E-687 data collection, Reduced Instruction Set Computer (RISC) chips, running at very large clock speeds, $\sim$100 MHz, were being made available to the workstation consumer at reasonable prices. Recognizing the potential and cost effectiveness of these machines Fermilab's Computing Division (CD) committed to purchasing large numbers of these CPU's to be used in distributed processing "farms" (see below), thereby addressing the requirements of data sets such as E-687's. Along with the hardware, the CD also developed a distributed computing environment, Cooperative Processes Software (CPS) and CPS Batch, which allow users to develop code which can run simultaneously on as many CPU's as desired. After a period of conversion of E-687 software to run under the UNIX operating system and CD debugging of the Farms environment, E-687 began using the Fermilab Farms in October 1991.

Farms Hardware

At the start of the Pass1 project, E687 had access to about 20 IBM RS6000 processors. This number steadily grew through the Spring of 1992 to as many as 60 machines combined between RS6000's and SGI 4D's. Generally, machines were grouped in units of "farmlets" containing between 8 and 12 machines. Reconstructing the data from one run, typically 600,000 events, required 14-16 hours of processing per CPU on a farm of 10 CPU's and at least 3 tape mounts. Often, a third output tape mount was required since the data set was being slightly more than doubled in size with both raw and reconstructed information being written. The CPU's were connected via an ethernet backbone and a shared file system. The logical structure of a farm is shown in Figure 4.4.

Software

In order to run Pass1 jobs on one of the Fermilab computing farms, the reconstruction software was modified to run in a distributed environment using the CPS package. CPS is a package of software tools that provides the ability to split computational tasks into logical units called User Processes (UP) and distribute these tasks over one or more computers. E-687 used 3 distinct processes, an input process (IP), an output process (OP), and a reconstruction process (RP). The input and output processes ran on one machine containing a pair of tape drives, while as many as 24 reconstruction processes ran on as many as 12 different machines. This

Figure 4.4: Fermilab farm structure.

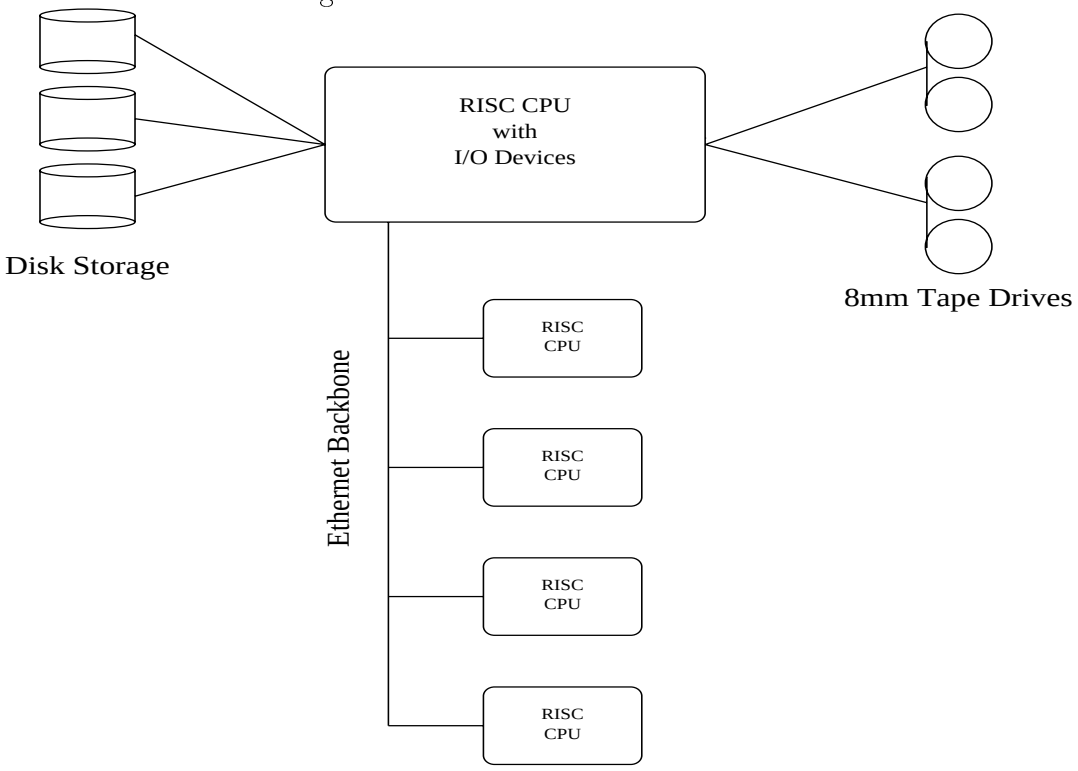

provided a huge increase in effective computing, thereby dramaticly shortening the total reconstruction time for the data set.

The primary tools for running CPS modified code are a Job Manager (JM) program, a Shared Memory Manager (SHM) program and the UP's. The JM and SHM are existing programs supplied with the Farm. The execution of the distributed job occurs by starting a JM process. The JM reads the Job Description File (JDF), which determines how many UP's to run and where to start them. E-687 typically started 1 input process, 1 output process, and 12 reconstruction processes. An example JDF is shown below.

```
CLASS=1
exabyte tapes = 1
number of processes = 1
PROGRAM=~e687/runp1/E687P1_IN.COM
CPU TYPE=AIX

CLASS=2
PROGRAM=~e687/runp1/E687P1_AN.COM
CPU TYPE=AIX
NUMBER OF PROCESSES=12
PROCESSES PER CPU =1

CLASS=3
exabyte tapes = 2
number of processes = 1
PROGRAM=~e687/runp1/E687P1_OUT.COM
CPU TYPE=AIX
```

The I/O processes ran on a specific node, while the reconstruction processes were started on all nodes in the farm. Once all the UP's are started, the JM starts one SHM on each CPU used. Communication between all UP's occurs via the

Figure 4.5: CPS Process Hierarchy.

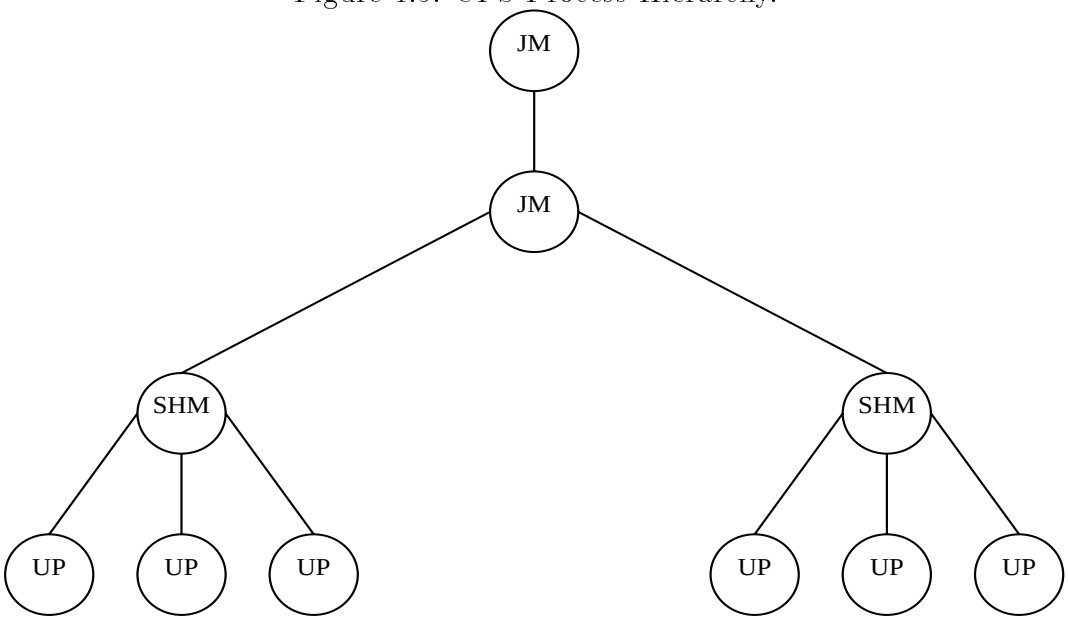

SHM's. The is accomplished by the UP's appropriately addressing a message and then passing it to the SHM. The SHM in turn passes this to the JM, which routes it to the appropriate SHM and on to the appropriate process. This hierarchy is shown in Figure 4.5. This method of communication allowed for the development of a process queuing system and a block data transfer system in CPS. These systems obviated the need for UP's to concern themselves with the state of other processes and thus minimized the modification of code used in a normal, one CPU situation.

Process queues allow a UP to temporarily suspend processing until an appropriate time in the future. This queued status is publicized to other UP's by putting the process identification number (PID) in the appropriate process queue. Another UP may "awaken" the queued process by requesting its PID from the appropriate

queue, and subsequently calling the routine. This type of queue usage is referred to as a "queue and call" system. If data is to be transferred between the calling routine and the dequeued process, then previous to the call, a data send must be made. This is accomplished through data transfer blocks. These blocks are defined by UP's, along with queue declarations during initialization. The send includes the PID of the receiving process, the data to be sent, and the block to use in the transfer.

E687 used a "queue and call" system for analyzing its data. The basic[1] system included the 3 process queues

- READY_QUEUE
- ANALYZED_QUEUE
- SYNCHQ,

along with the 2 data transfer blocks

- IN_BLOCK
- OUT_BLOCK.

The reconstruction process began by the initialization of each of the UP's performing the necessary tasks to prepare for the analysis cycle. Once this initialization was complete each UP queued itself on the SYNCHQ, signaling to the input process that

[1] There were 4 other blocks used, but these were ancillary to the reconstruction algorithm and are omitted from this discussion.

the analysis cycle could proceed. The E-687 analysis cycle began when the Input Process (IP) read an event buffer and dequeued a Reconstruction Process (RP) from the READY_QUEUE. The IP then sent the event buffer through the IN_BLOCK transfer block, and invoked the RP with a "call". This call starts the reconstruction process and also instructs the RP to return itself to the READY_QUEUE upon successful completion. After the call to the RP, the IP read another input buffer and repeated the logic just described. Meanwhile, the RP executes the reconstruction phase and after successful completion, dequeues the Output Process (OP) from the ANALYZED_QUEUE queue. Since there was only one OP, this dequeuing request meant the RP had to wait for the OP to become available which was signaled by presence of the OP on the ANALYZED_QUEUE. The RP then sent the output data through the OUT_BLOCK transfer block and called the OP. In the call to the OP, the RP was instructed by the OP to wait for the return of the OP from the tape write. This provided a mechanism for cleanly shutting down all UP's in case of fatal tape errors. Once the OP returned without error, the RP requeued the OP on the ANALYZED_QUEUE, and requeued itself to the READY_QUEUE as instructed. This process is summarized in Figure 4.6.

To facilitate the use of the farms a batch queue system was developed to allow for multiple job submission, and thus 24 hours per day processing. Jobs were submitted to the batch queue using the **cps_submit** command, with the Job Description File, Job Control File (JCF) and Farm name as parameters. The JCF

Figure 4.6: E-687 Queue and Call Reconstruction Flow-Chart.

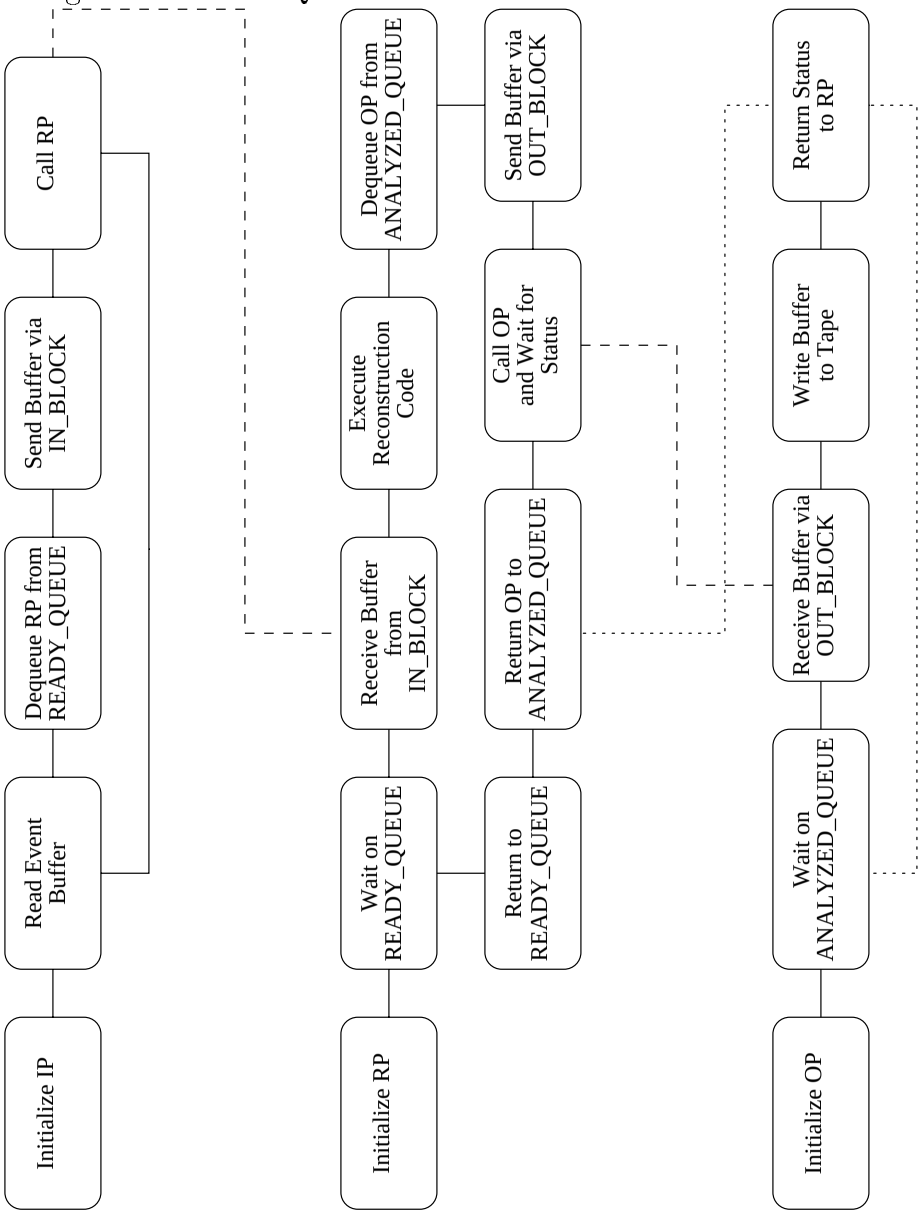

supplied the following information about a CPS batch job.

- Names and order of tapes that will be needed by each class of processes.
- Job Manager input data files, *i.e.* the User Processes, to be copied to the remote systems where the CPS batch job will run.
- Output files to be retrieved after a job completes.
- Directories where the output and the log files should be placed.

An example JCF file is shown below.

```
class = 1
tapes(1,input,exabyte) = yd7880
output directory = runp1/results/job7880a
data file = ~e687/runp1/rt687_in.exe
output file = RN*
output file = rti*
output file = rn_rz.hbka
output file = oddp.dat
class = 2
output directory = runp1/results/job7880a
data file = ~e687/testp1/rt687_an.exe
class = 3
output directory = runp1/results/job7880a
data file = ~e687/runp1/rt687\_out.exe
otapes(1,output,exabyte) = yv7880,yv4880,yv1111
output file = rto*
```

Since each job required a customized JCF, a UNIX shell script, **p1_submit**, was written to create the JCF and issue the **cps_submit** command. Along with creating the JCF, a directory to house the output from the various UP's was also created during each submission. Input parameters for **p1_submit** include the raw

data tape label, an overflow output tape and a serial identification for the job. Raw data cassettes were designated by the prefix YD while YV tapes denoted the reconstructed output tapes. For each photon data tape (*e.g.* YD7860), two output tapes were assumed to be necessary (*e.g.* YV7860, YV4860). Occasionally a third tape was required and was included in the submission. The serial identification was used in case a job crashed before all events were reconstructed. Resubmissions were handled as new jobs, with the **p1_submit** routine creating new output directories and possibly specifying new output tapes. Since it was not uncommon for a Pass1 job to crash during the middle of a job, a check point procedure was included to avoid starting the reconstruction at the beginning of the tape. Each time the IP read an E-687 file marker, a message was placed in the IP output log. When a job was resubmitted the IP log from the preceding serial, if it existed, was searched for file marks, and the new job started reconstruction from the last completely read file. It was not uncommon for a reconstruction job to be submitted as many as 4 times. Tape hardware errors were a primary cause, as were the numerous early bugs in the CPS and CPS Batch software.

To ensure a continuous reconstruction of the data, several jobs were submitted at one time, enough to ensure at least 24 to 36 hours of computing. If something drastic were to happen on a particular farm, causing the batch queue to drain, system operators at Feynman Computing Center were instructed to notify the Pass1 shift person on duty. To allow for the mobility of Pass1 shift personnel, a pager

Table 4.1: Pass1 Summary Statistics

Number of Events	1990	1991	Total
Read	275,016,917	211,030,666	486,047,583
Written	204,259,613	160,628,066	364,887,679

system was used. The Fermilab CD provided a pair of "sky-pagers," which allowed movement throughout the United States. A series of codes were sent via the pager to the Pass1 shift person, specifying the which farm was affected and the severity of the problem. This allowed for an appropriate response by the Pass1 crew.

After a reconstruction job successfully completed, all generated output, including log files, monitoring histograms, and reconstruction statistics were archived using the Fermilab VAX cluster archiving utility. The process of archiving this information was accomplished by using a DCL command procedure, **P1_FETCH.COM**. This routine copied all files associated with a job into the E-687 project area. Subsequently, the log files, monitoring histograms and node statistics were combined into a backup saveset and archived. After archival, some of the monitoring histograms and statistics were combined into a running total. Finally an ASCII file database used to monitor Pass1 progress was updated. A typical set of monitoring histograms is shown in Figure 4.7 and a summary of Pass1 statistics are shown in Table 4.1.

As mentioned previously, the Pass1 project began in October 1991. The

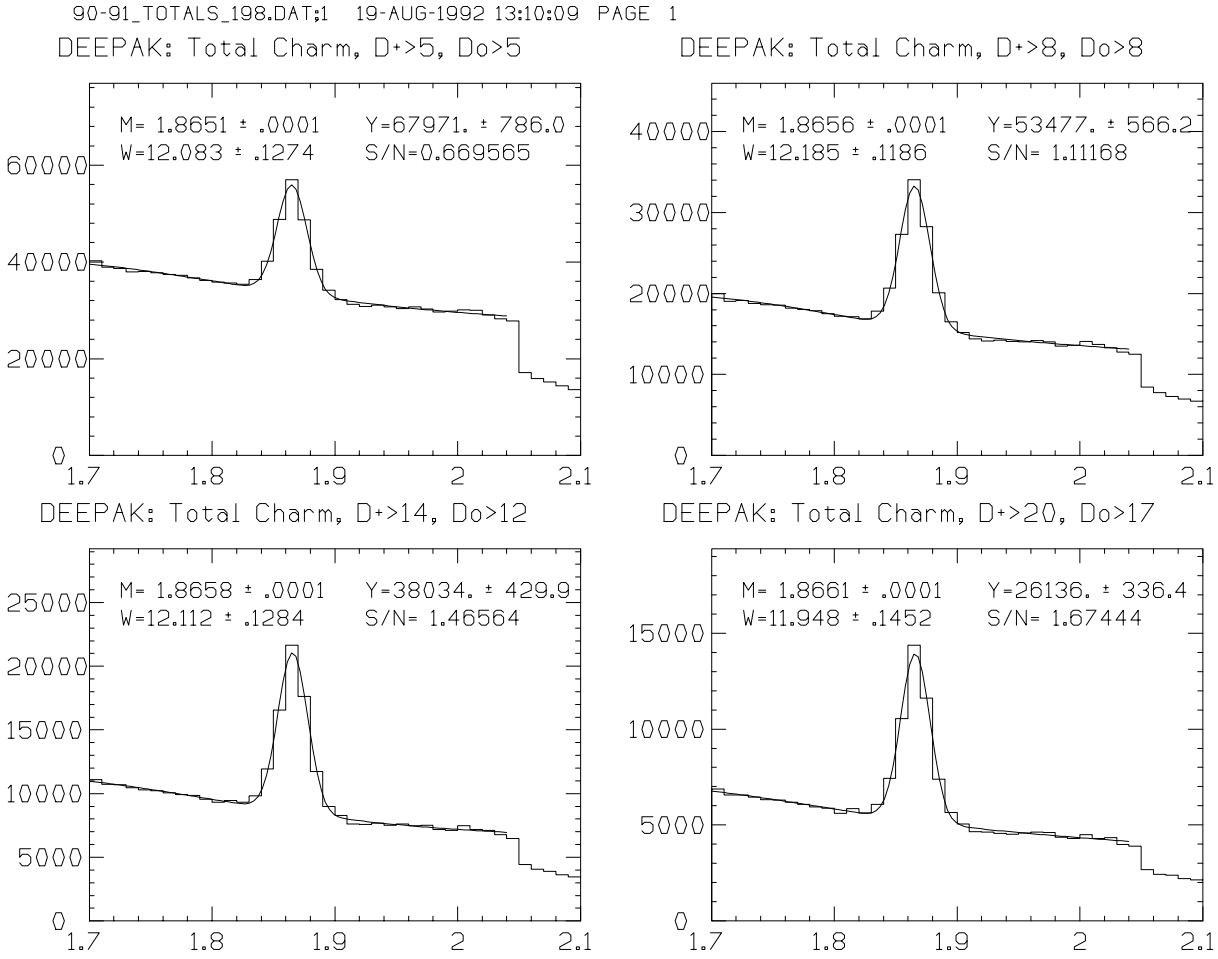

Figure 4.7: Results of Pass1 Charm Yield Monitoring.

project ran continuously for approximately 10 months, until August 1992. Over 350,000,000 events were analyzed and written to tape with close to 5 Terabytes of data being stored as output. The project required the efforts of 8 graduate students and on order of 200 VAX–780 years of computing to complete.

4.3.2 Track Reconstruction

As described in the previous chapter, the E-687 spectrometer used two tracking systems, the microstrip system and the MWPC system. Since the acceptance for certain decay daughters is different for each of these regions (*e.g.* $K_s^0 \rightarrow \pi^+\pi^-$), the track reconstruction algorithms for each system work independently. After separate track reconstruction, linking of all possible microstrip and MWPC tracks was performed.

Microstrip Region

The microstrip track finding algorithm is a projection based algorithm using each of the views separately. This greatly improves the speed of the reconstruction and since the maximum angular error provided by the granite support is $\sim 6 \times 10^{-5}$, the efficiency of this algorithm is quite high.

Before the projection algorithm is invoked, clusters of adjacent hits in each view are created and the total integrated charge is used to estimate the number of charged particles passing through the cluster. These clusters are then used to create

"track projections" in each view, requiring at least 3 of the 4 planes measuring the particular view to have fired. Since momentum information is not available, the cuts on the projections are relatively loose. Hits of the last three stations, already assigned to a track having hits on all four stations, cannot be reused for a new track with only three hits.

After the track projections are created, they are formed into tracks. If they match in space and have a global χ^2 per degree of freedom lower than 8. Tracks sharing one or two projections are then arbitrated based on their χ^2. The process is performed in a symmetric way, *i.e.* only the best j and k projections are used for a particular i projection, and then permuted to find the best i and j associations for the k projection.

After all 3-4 plane microstrip tracks have been formed, hits not associated with these tracks are used to search for wide angle tracks. Instead of using projections, space points are formed from the remaining hits. These space points are then used to form a track. At least 6 hits are required for the track.

The reconstruction efficiency of this algorithm was checked by a $D\bar{D}$ Monte Carlo simulation using the measured hit efficiencies of the microstrip detectors, including hot and dead strips. This overall track reconstruction efficiency was measured to be 96%, including the effects due to multiple coulomb scattering. The relative percentage of reconstructed spurious tracks is $\sim 2.7\%$. Figure 4.8 shows the track reconstruction efficiency as a function of track momentum.

Figure 4.8: Efficiency of microstrip track reconstruction algorithm.

Figure 4.9: Linking efficiency of microstrip and MWPC tracks. a) 3-Chamber tracks. b) 5-Chamber tracks.

MWPC Region

The tracking algorithm used in the MWPC's is very similar to the microstrip system. It is also a projection based algorithm. Tracks can be formed using 3, 4, or 5 chambers. In these cases, the eventual track must contain a hits in P0. The reconstruction begins by forming projections in each of the 4 views (U,V,X and Y). In all but the X views, projections are formed from the MWPC information alone. The X view is seeded by projecting the existing microstrip tracks into P0 and matching hits. The tracks are then formed by matching the 4 views. After all microstrip projected tracks are found, new X projections are created using just MWPC's hits. These are then matched with unused U,V, and Y projections to form additional tracks. All tracks were fit using a least-squares method. The fit parameters were the intercepts and slopes of the X and Y views (x_0, y_0, x', y') in the M2 coordinate system. If the track traversed all 5 chambers, then a 5th parameter, the change in Y slope, $\delta y'$, between the segments upstream and downstream of M2 was included. Tracks were not permitted to have more than 4 missing hits among all chambers used and at least 2 hits in each chamber. A χ^2/DOF cut was also used.

To improve the quality of the fit for 5 chamber tracks, a momentum was assigned based on $\delta y'$ and the sudden bend approximation. This allows for further refinement to the momentum measurement by considering the fringe fields in M1 and M2 extending beyond the pole tips into the tracking regions. Also, off-field

components (B_y, B_z) of the magnetic field can be corrected for in the fit. These corrections are included by iterating each 5-chamber track through a fit using all this information. The track momentum is then adjusted each iteration until it is stable. Tracks passing only through the P0, P1 and P2 do not yet have information that can be used to assign momentum.

To recover track topologies not covered by the main reconstruction routines, several other routines are available. These include extending microstrip tracks into the MWPC system. The microstrip track parameters are used to predict the location of hits in P0 and P1. If hits match and the selected deviation from the predicted extension is less than 2 wires, the track is refit. This least-squares refit is performed using all hits in both systems and the MWPC fit parameters determined.

The efficiency of the MWPC reconstruction algorithm was studied in a similar way as the microstrip system. The efficiency was determined to be greater than 98% for tracks with a momentum exceeding 5 GeV/c. Due to the presence of MWPC system oscillations during data taking, and to reduce the time required to reconstruct all tracks in this type of event, a limit of 30 MWPC tracks was imposed.

Linking

Once charged particle tracks are found in both the microstrip and MWPC tracking systems, an attempt to link these tracks is made. This process is vital for properly constructing vertices (the basis of most E-687 analyses and which will be explained

in detail iu the next chapter) as complete error information on microstrip tracks is lacking without momentum information. It can also be significant if a MWPC track does not link, *e.g.* a possible sign of Λ and K_s^0 decays.

The linking algorithm begins by extrapolating microstrip and MWPC tracks into the center of M1. If a microstrip track and a MWPC track are found which have the same X intercept and X slope at the M1 center, they form a candidate link. This process allows for multiple MWPC tracks to be linked to the same microstrip track in the first pass. A global least squares fit using all hits from both segments of the new track is performed. If there are more than one MWPC tracks linked to a microstrip segment, then an arbitration is performed based on the χ^2 per degree of freedom. After arbitration, no more than two MWPC tracks are allowed to be linked to a single microstrip track. Two MWPC tracks are allowed to link to a single microstrip track, since e^+e^- pairs are often produced with unresolvable opening angle in the microstrip detector, and reconstruct as a single track in this region. Figure 4.9 shows the linking efficiency as a function of momentum.

Momentum Determination

Momentum determination is one of the single most important measurements made in E-687. Since many of the errors calculated in track and vertex fitting are momentum dependent, accurate knowledge of a track's momentum is imperative for producing meaningful physics results. There are several different approaches used, depending

on track topology, for measuring the track momentum. For 5-chamber tracks, the momentum is calculated by tracing the track through the magnetic field of M2. The trace uses the track parameters upstream and downstream of M2, along with the magnetic field information as stored in the magnetic field map, (which includes fringe fields). The momentum that results from the trace is then fed back into a least squares fit of the track, and new track parameters are calculated. This process is iterated until the track's parameters reach a point of stability.

For 3-chamber tracks, a link to a microstrip track is required to measure its momentum. The basic algorithm is the same as the 5-chamber track, except the M1 magnetic field is used and the microstrip segment P0-P2 segment must obviously be used during the track parameter refit. Tracks which have hits in chambers P0, P1, P2, and P3 are treated in an identical manner.

Unlinked 3-chamber tracks, *i.e.* "stubs," are the only type of track for which momentum information cannot be calculated without some type of assumption. For these tracks the assumption is made that the closest vertex which the stub extrapolates back to in X is the production point. From this point the tracing algorithm is invoked to produce the track parameters measured downstream of M1. If no reasonable vertex is found, then the track is assumed to have been produced at the center of the target.

The momentum resolution for tracks whose momenta were determined in M1 or M2 are

$$\frac{\sigma_p}{p} = 3.4\% \left(\frac{p}{100GeV/c}\right) \sqrt{1 + \left(\frac{17GeV/c}{p}\right)^2} \quad (4.2)$$

$$\frac{\sigma_p}{p} = 1.4\% \left(\frac{p}{100GeV/c}\right) \sqrt{1 + \left(\frac{23GeV/c}{p}\right)^2}, \quad (4.3)$$

where p is in units of GeV/c.

4.3.3 Čerenkov Identification

E-687 uses three Čerenkov detectors operating in threshold mode to identify charged hadron tracks with a known momentum. Electron and positron tracks are identified in the Electromagnetic calorimeters while muons are identified by the Muon system. The Čerenkov identification starts by tracing a track through each of the three detectors and determining the cells for which light should be either present or absent. In each detector, the cell which the track traverses and its adjacent cells are used to determine the total amount of light present in the detector due to the track. If this light is above the pedestal value for background, then the cell is considered to be "on." A three-bit binary pattern is the assigned to each track according to the absence (0) or presence (1) of light in the appropriate cells. This pattern is then compared to the pattern that would be produced by a hypothetical electron, pion, kaon or proton of the same momentum. The hypothesis for each matching pattern is returned in a four-bit code referred to as the **ISTATP** code. For example, if a 35 GeV/c kaon passes through all three Čerenkov counters, then using Table 3.4 the

Table 4.2: Čerenkov hypotheses and **ISTATP**.

Particle Identification	**ISTATP** Code
Inconsistent Info.	0
$e^{\pm}$	1
$\pi^{\pm}$	2
$e^{\pm}$ or $\pi^{\pm}$	3
$K^{\pm}$	4
$e^{\pm}$, $\pi^{\pm}$, or $K^{\pm}$	7
p	8
$K^{\pm}$ or p	12
$\pi^{\pm}$, $K^{\pm}$ or p	14
$e^{\pm}$, $\pi^{\pm}$, $K^{\pm}$ or p	15

binary pattern representing the expected light pattern would be 110, where C1 is the most significant bit, and C3 is the least significant bit. The patterns expected for a pion or proton are 111 and 010, respectively. Thus, for this momentum, the kaon can be uniquely identified and the binary **ISTATP** code of 0100, or decimal 4 is assigned. If the kaon had a momentum of 50 GeV/c, then the binary light pattern expected would be the same as above, but now the pattern expected for the proton would also be 110. Thus, a unique identification is no longer possible, and there for the binary **ISTATP** code of 1100, or decimal 12 is assigned. Table 4.2 lists the particle identification hypotheses and decimal **ISTATP** codes observed in E-687 data.

4.3.4 Skims

Subsequent to the reconstruction of an event, several routines were run to classify the event based on its physics potential. Each of these routines are referred to as a "skim" and if the criteria of a particular skim were met, the event was flagged by setting a "skim bit." This bit was part of a 32-bit word of data which described the results of each skim, i.e. 0 – failure, 1 – success. This allowed for fast, post reconstruction filtering of the Pass1 output.

The skim used for the the current work is referred to as the "Global Vertex" skim. This is a general purpose skim intended to provide a sample of events with at least two vertices detached in space by a statistically significant amount. Since heavy quark weak decays are characterized by this type of topology, events contained in this sample provide an enriched charm sample from which to begin a subskim. The Global Vertex skim code operates by combining pairs of linked microstrip tracks and attempts to form a vertex. Details of the vertex reconstruction are presented in the next chapter. To briefly summarize a χ^2 minimization of the point of closest approach for the pairs of tracks is performed, and the resulting χ^2 is used to calculate a confidence level. All vertices used in the Global Vertex skim are required to have a confidence level greater than 1%. If an event contains at least two vertices separated in z (beam direction) by more than $4.5\sigma_z$, where σ_z is the error on the separation, then it meets the Global Vertex requirement. The minimum number of linked

microstrip tracks required for these event is three. The entire reconstructed E-687 data set which met at least one skim requirement and written in a data summary format is saved on over 150 8mm data cassettes and is comprised of $\sim$ 365 million events. The Global Vertex skim, written in the same format is saved on 24 8mm tapes, and contains $\sim$ 15 million events.

Chapter 5

Analysis of $K^-\pi^+\pi^-$ Decays

The analysis of $K^+\pi^-\pi^+$ decays began where the Pass1 reconstruction and skimming of the E-687 data set left off. The analyses presented here were derived from the Global Vertex skim described in the previous chapter and then analyzed using the software analysis tools developed by the E-687 Collaboration. This chapter describes relevant notation, techniques, tools, and algorithms used to calculate the branching ratios presented.

5.1 Candidate Driven Vertexing

At the core of almost all analyses performed by E-687 experimenters is SDVERT, a candidate driven vertexing package[33]. Tracks passing through the microstrip detector system typically have a transverse (to the beam direction) error at the

center of the target of $\sim 10\mu m$. With this high degree of precision, it is possible to uniquely reconstruct the decay vertex of a charm particle using its daughter tracks, and then using the resultant three–momentum, extrapolate upstream to "seed" the charm production vertex. This process is referred to as "candidate driven vertexing." Once these vertices are found, it is possible to calculate the relative isolation from other tracks and vertices in the event, which can be used to reject both physics backgrounds and combinatorial backgrounds.

5.1.1 Charm Production and Decay Vertices

The process of reconstructing the decay chain $D^+, D_s^+ \rightarrow K^+\pi^-\pi^+$ begins with the reconstruction of the $K^+\pi^-\pi^+$ vertex. Microstrip tracks, uniquely linked to MWPC tracks satisfying the appropriate particle identification requirements, are combined into a candidate vertex. The vertexing algorithm works by minimizing the transverse distance of closest approach of the candidate tracks involved in the decay. Under this assumption, the χ^2 of a vertex with N tracks is

$$\chi^2 = \sum_{i=1}^{N} \left(\frac{x_v - (x_i + x_i' z_v)}{\sigma_{x,i}} \right)^2 + \left(\frac{y_v - (y_i + y_i' z_v)}{\sigma_{y,i}} \right)^2 . \quad (5.1)$$

The quantities x_i, x_i', y_i, and y_i' are the track parameters of the ith track. The quantities $\sigma_{x,i}$ and $\sigma_{y,i}$ are the extrapolation errors of the ith track and include the effects due to multiple Coloumb scattering. The quantities x_v, y_v, and z_v are the fit parameters for the vertex position. Once the χ^2 minimization has been performed,

the value of the χ^2 can be used to calculate a confidence level for the vertex fit. For decay vertices, this confidence level is referred to as DCL, and typically vertices with a DCL less than 1.0% are rejected.

The production vertex is reconstructed by combining the decay vertex daughter tracks into a D momentum vector which intercepts the the decay vertex. From this information, a complete set of track parameters is calculated, including the associated error matrix. Since the production vertex must be intercepted by the candidate "D track," unused tracks in the event are clustered around the "D track" to form a candidate production vertex. A χ^2 fit similar to the above is performed and the production vertex confidence level, PCL, is used to reject tracks that don't belong to the production vertex. If the confidence level of the vertex fit drops below 1% when a new track is added to the fit, the track is rejected. If no tracks are found which create a vertex with PCL greater than 1%, then the candidate *decay* vertex is rejected.

Once suitable production and decay vertices have been found, their spatial separation can be calculated. Since tracks used in vertex fits are required to have complete error information, including the effects due to multiple Coloumb scattering, the error on this separation can be accurately found. The separation divided by its error, ℓ/σ_ℓ, allows for a statistically significant measurement of the distance a candidate D has traveled before decaying. The error is calculated by adding the production and decay vertex position errors in quadrature. For a D^+ candidate in the

E-687 spectrometer, the mean distance of travel is approximately 1.5cm, which corresponds to $\ell/\sigma_\ell \sim 20$. This quantity is very useful in rejecting backgrounds which don't have a charm proper lifetime and includes non-charm events and hadronic reinteractions of charm daughters in the target.

Another technique for dramatically reducing contamination due hadronic reinteractions is to require the decay vertex to lie outside the target. With the known position of the target, the separation of the decay vertex from the downstream end of the target in units of its error, ℓ_v/σ_{ℓ_v}, can be used to ensure that the decay occurs outside a dense medium. This reduces the probability that a daughter track will suffer a nuclear interaction and dramatically improves the signal to noise ratio of the decay of interest. Due to the design of the E-687 target as a single $\sim$ 4cm long Be block, this quantity is only useful for the longer lived charm states.

5.1.2 Vertex Isolation

Since reconstruction of the decay vertex requires that candidate tracks are included at a set confidence level, backgrounds arise from real vertices which have multiplicities different from the vertex being reconstructed. Two classes of such backgrounds are identified. The first class results from tracks which originate at the production vertex and follow the D, thereby increasing the decay vertex multiplicity. This is common in $D^{*+} \to D^0\pi^+$ decays where the Q of the decay is just 39 MeV/c. The π^+ from this decay often travels along the D^0 direction. The second class results

from higher multiplicity vertices where the candidate decay vertex is built from a subset of tracks in this vertex.

To reject these backgrounds two tests of "vertex isolation" are performed. The first test rejects backgrounds of the first class by refitting the primary vertex and individually including the decay vertex daughters. The largest vertex confidence level from each of these fits, referred to as ISO1, is a measure of the relative isolation of the primary vertex from the secondary daughters, or the significance of the of daughter "point-back." This confidence level is very dependent on the Q of the decay being considered and the level of rejection varies accordingly.

The second class of backgrounds is rejected by individually refitting the decay vertex with each track in the event not already assigned to either the production or decay vertices. The largest confidence level, referred to as ISO2, which results, is a measure of the isolation of the secondary vertex from other tracks in the event. Typically, a decay vertex is rejected if the ISO2 confidence level exceeds 1%.

5.2 Particle Identification Mnemonics.

As was explained in the previous chapter, the particle identification for each track reconstructed was performed by comparing the response of the Čerenkov counters to the response expected for hypothetical particles of the same momentum. A four-bit code, **ISTATP**, is returned representing which of the four hypothetical particles

Table 5.1: Mnemonics for **ISTATP** Codes.

Mnemonic	**ISTATP** Codes	Candidate Particle
NHE	0,2,3,6,14,15	Pions
PIDEF	2,3	Pions
KP	4,12	Kaons
KP7	4,7,12	Kaons
KP8	4,8,12	Kaons
KP78	4,7,8,12	Kaons

could have produced the Čerenkov system response. To avoid the confusion of using a notation based on **ISTATP** codes, a mnemonic system has been employed which is suggestive of the nature of the particle identification returned by the Čerenkov system. For the analyses considered here, the mnemonics used to represent the **ISTATP** codes that a track may satisfy, as listed in Table 4.2, are shown in Table 5.2. For example, a track is considered to pass the **ISTATP** cut of KP if the track's **ISTATP** code is either 4 or 12.

5.3 The $D^+ \to K^+\pi^-\pi^+$ Analysis.

5.3.1 The Subskim

As was mentioned, the $K^+\pi^-\pi^+$ analyses were derived from the Global Vertex skim. To reduce the data set further, a physics specific subskim was performed. The skim made strict topology requirements along with some loose particle identification

requirements to bring the analysis sample to a manageable size. The skim began by classifying tracks according to particle species and link status. When searching for charm decay vertices, only singly linked tracks were used. This requirement did not exist for charm production vertices, but at least 2 microstrip were required in the production vertex. Each PWC track was also checked as to whether the **ISTATP** Kaon bit was set and thereby consistent with the Kaon hypothesis. From these sets of tracks, the subskim algorithm searched for candidate decays by forming a three-track charm decay vertex, containing at least one kaon consistent track, and having a confidence level greater than 1%. The total charge of the vertex was required to be ± 1. The production vertex was then seeded and was required to have a vertex confidence level greater than 1%. Further, the separation of the production and decay vertices was required to have ℓ/σ_ℓ greater than 3. To reduce the number of candidate events even further, $K\pi\pi$, $KK\pi$, and KKK invariant mass was calculated. If none of these masses fell within the window of 1.7 GeV/c^2 and 2.1 GeV/c^2 the event was rejected. This subskim reduced the data set to approximately 1.4 million events, which were easily stored on a single 8mm data cassette. To check for a bias in the skim, a Monte Carlo generated data set was used. The Monte Carlo data were reconstructed with and without the subskim requirement. The left plot in Figure 5.1 shows the reconstructed mass for 5×10^5 generated $D^+ \to K^+\pi^-\pi^+$ decays without the skim requirement, while the right plot required the skim.

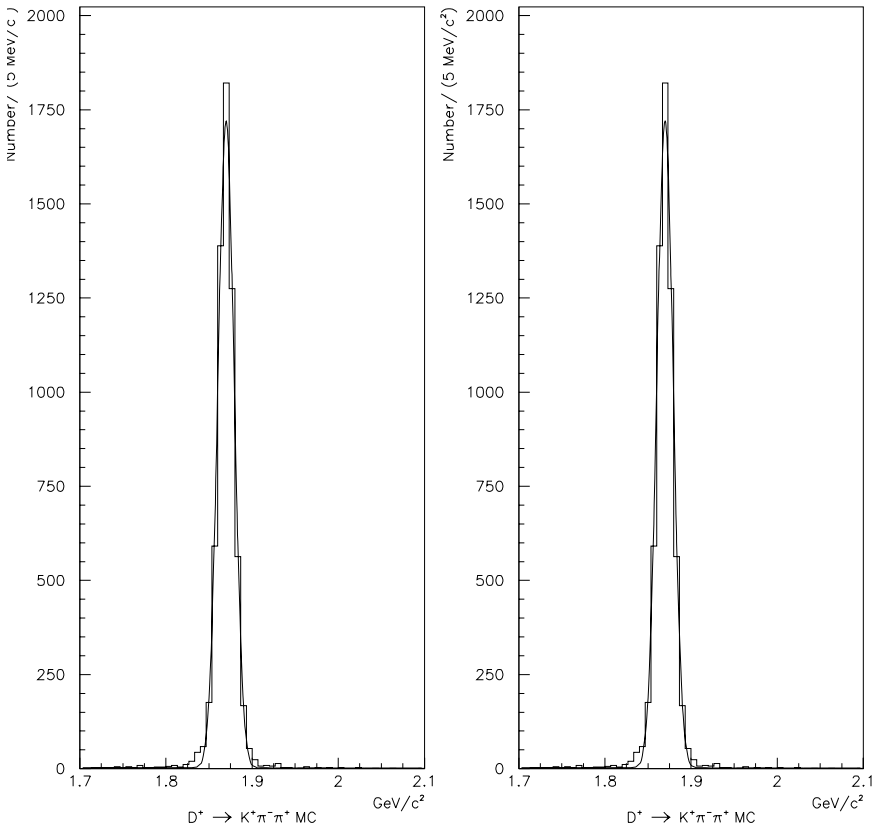

Figure 5.1: 5×10^5 generated $D^+ \to K^+\pi^-\pi^+$ decays. a) Events not passed through analysis skim. b) Events satisfying analysis skim requirements. Total yield for both plots is 6022 ± 92 events.

5.3.2 Cuts for the D^+ Analysis

After the subskim, determination of the appropriate cuts for measuring the $K^+\pi^-\pi^+$ branching ratio was performed. A simple estimate of the number of possible doubly Cabibbo suppressed decays can be calculated by using equation 1.6 on page 4. Assuming it is possible to obtain a sample of approximately 10,000 background free $D^+ \to K^-\pi^+\pi^+$ decays, then it is possible to observe roughly 30 $D^+ \to K^+\pi^-\pi+$ decays. Thus, to determine the best set of cuts for the measurement of interest the "sensitivity" of the $K^-\pi^+\pi^+$ decay was optimized. Sensitivity is defined as,

$$\xi \equiv \frac{Y}{\sqrt{B}} \simeq \sqrt{S_n \cdot Y}, \tag{5.2}$$

where Y is the signal yield, B is background beneath the signal, and S_n, is the signal-to-noise. The cuts to be optimized for this analysis were the particle identification cuts of both the pions and kaons, the isolation cuts of the primary and secondary vertices, ISO1 and ISO2, the separation of the production and decay vertices and the position of the decay vertex in the target. Figure 5.2 shows the trajectory of the sensitivity curves in the $K^-\pi^+\pi^+$ signal yield and inverse sensitivity space as the ℓ/σ_ℓ cut is varied through the points 5, 10 15, 20, and 25. The legend describes the value of the cuts used for each curve, and the notation "Vac." corresponds to a cut of $\ell_v/\sigma_{\ell_v} > 1.5$. The region of best searching power for the $K^+\pi^-\pi^+$ signal is where the inverse sensitivity and the yield are minimized. Table 5.2 shows the set of cuts which meet this criteria.

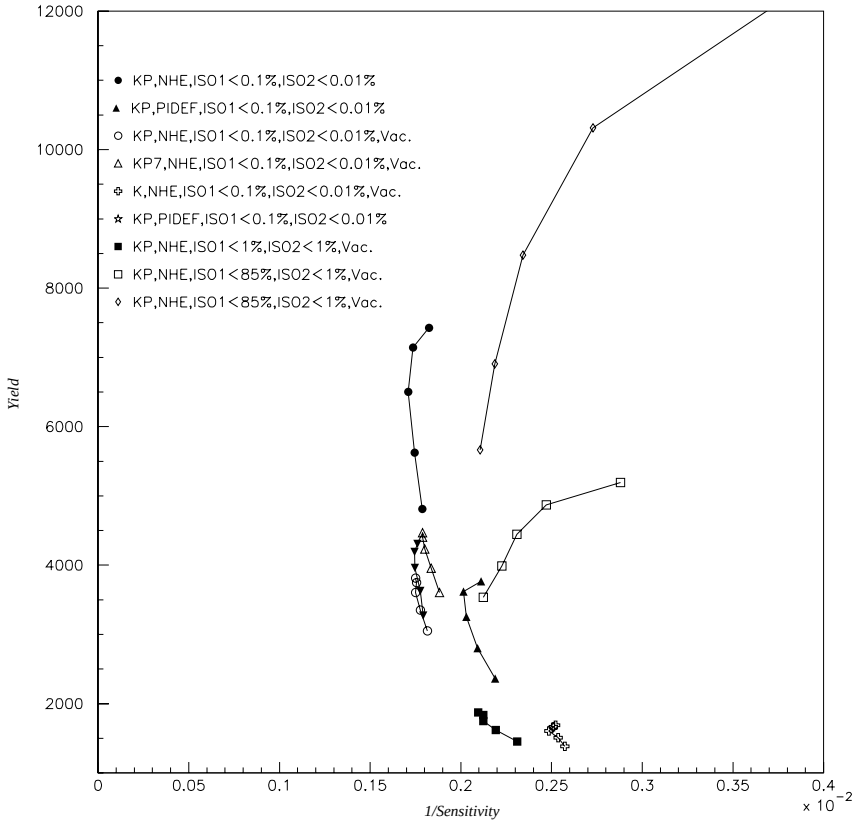

Figure 5.2: Sensitivity studies using the $K^-\pi^+\pi^+$ signal from data.

Table 5.2: Sensitivity Optimized Cuts

Cut	Value
Kaons	KP
Pions	NHE
DCL	$> 1\%$
ISO1	$< 0.1\%$
ISO2	$< 0.01\%$
ℓ/σ_ℓ	> 15
ℓ_v/σ_v	> 1.5

Along with these cuts, the following set of baseline cuts were employed,

- The production vertex contained at least 2 microstrip tracks.
- The production vertex confidence level (PCL) greater than 1%.
- The decay vertex was required to lie upstream of the TR1 counter.

The production vertex multiplicity requirement assures a statistically correct calculation of ℓ/σ_ℓ, as the error on this vertex is determined from the error on the vertex fit without the candidate "D track" included. Due to the algorithm used to find the production vertex, PCL does not represent the best fit vertex to be found and cutting on this is statistically meaningless. The requirement that the decay vertex lie upstream of the TR1 counter was necessary since the Monte Carlo simulation of these decays did not allow for charm production downstream of the target.

Figure 5.3 shows the $K^+\pi^-\pi^+$ and $K^-\pi^+\pi^+$ invariant mass distributions for the above cuts. The $K^+\pi^-\pi^+$ distribution was fit using two Gaussian peaks added to a polynomial background shape. The D^+ mean and width were constrained to the values determined from fitting the $K^-\pi^+\pi^+$ distribution, while the D_s^+ mean and width were determined by Monte Carlo studies. The $K^-\pi^+\pi^+$ distribution was fit with a single Gaussian peak added to a polynomial background shape.

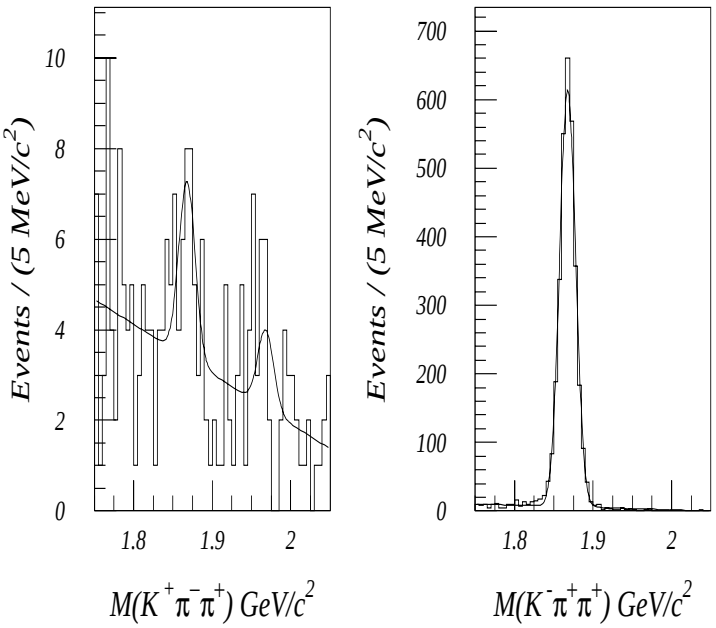

Figure 5.3: $K^+\pi^-\pi^+$ and $K^-\pi^+\pi^+$ invariant mass distributions. The D^+ yields are yields are 20.9 ± 6.6 and 2903 ± 62 events.

5.3.3 Consideration of Backgrounds

There are several charm backgrounds which may contribute to the $D^+ \to K^+\pi^-\pi^+$ signal. For example, if the K^- from a $D_s^+ \to K^+K^-\pi^+$ decay is mis-identified as a pion, then the corresponding $K^+\pi^-\pi^+$ invariant mass may fall in the D^+ region. The presence of apparent $D_s^+ \to K^+K^-\pi^+$ decays is shown in Figure 5.4. Both plots in the figure are $K^-K^+\pi^+$ invariant mass distributions formed by changing the appropriate mass assignments of the $K^+\pi^-\pi^+$ candidates shown in Figure 5.3. The left plot uses all possible $K^+\pi^-\pi^+$ candidates and the right plot uses just those candidates whose $K^+\pi^-\pi^+$ invariant mass falls within $\pm 2\sigma$ ($\sigma = 10MeV/c^2$) of the accepted D^+ mass[1]. Although the left plot appears to show the presence of $K^+K^-\pi^+$ decays in the $K^+\pi^-\pi^+$ data stream, it is clear from the right plot that the amount of this contamination in the $K^+\pi^-\pi^+$ signal is slight. Attempts to determine the amount of this contamination by fitting the right histogram results in yields which are statistically consistent with zero. In another attempt to quantify this background, a Monte Carlo sample was generated and passed through the $K^+\pi^-\pi^+$ analysis. This sample was generated containing at least one D_s^+ and any other other charm-bar species. All known charm species and their respective decay modes are generated. This provides an enriched sample of D_s^+ decays from which to study downward reflection into the D^+ signal region. The resulting $K^+\pi^-\pi^+$ invariant mass plot is shown in Figure 5.5. The generated Monte Carlo

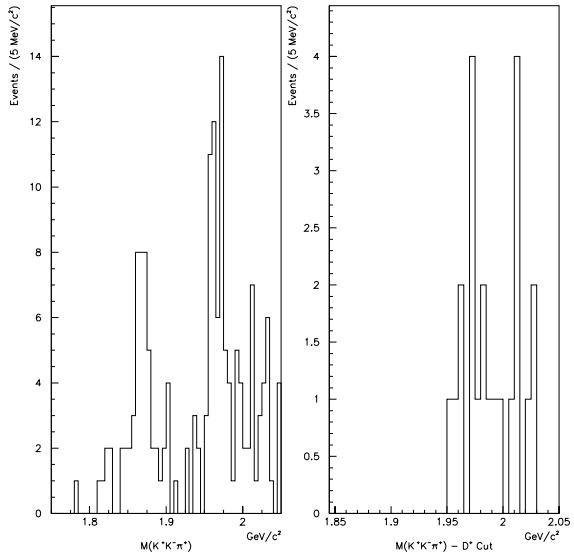

Figure 5.4: $K^+K^-\pi^+$ invariant mass distributions in $K^+\pi^-\pi^+$ invariant mass distribution. The right plot uses $K^+\pi^-\pi^+$ candidates from $\pm 2\sigma$ of the accepted D^+ mass. See text for complete description.

sample represents 6 times the 90-91 data set, and so the histogram was scaled to represent the true contribution to $K^+\pi^-\pi^+$ signal. A binned likelihood fit using a Gaussian peak added to a simple polynomial gives 1.8 ± 2.3 D^+ events. Given, this poor statistical significance and the difficulty in observing this reflection in the D^+ region, no correction from this background was made, but the error on the estimate will be used as a systematic uncertainty..

Another background to be concerned with is the doubly mis-identified $K^-\pi^+\pi^+$ signal. The left plot in Figure 5.6 shows the $K^-\pi^+\pi^+$ signal that results from $K^+\pi^-\pi^+$ events within $\pm 2\sigma$ of the accepted D^+ mass. Also shown are

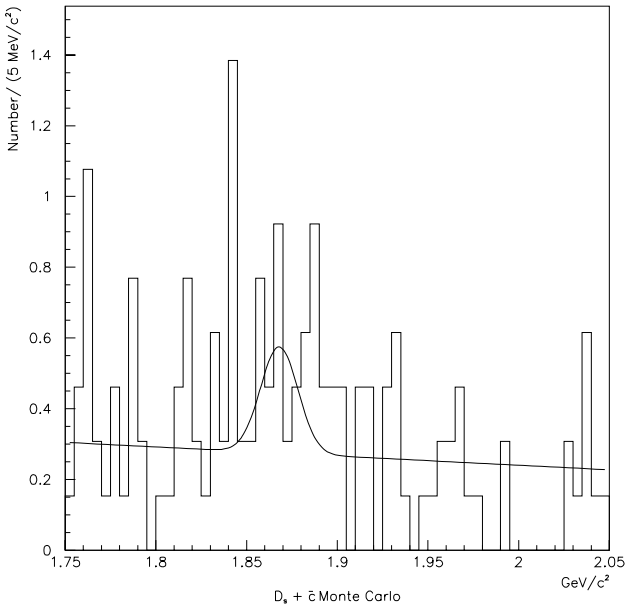

Figure 5.5: The left figure contains $K^+\pi^-\pi^+$ events from a $D_s^+ + \bar{c}$ Monte Carlo scaled to data. The fit yield is 1.8 ± 2.3 D^+ events.

the $K^+\pi^-\pi^+$ events which have a $K^-\pi^+\pi^+$ mass within $\pm 2\sigma$ of the D^+. This distribution does not show any peaking near the D^+ mass.

Finally, one other explicit background was considered. The decay $D^+ \rightarrow K^+K_s^0$ is singly Cabibbo suppressed. If the K_s^0 decays into a dipion pair almost immediately after the D^+ decay, it might be possible to reconstruct this event as a $K^+\pi^-\pi^+$ candidate. Figure 5.7 shows the $\pi^+\pi^-$ invariant mass distribution from $K^+\pi^-\pi^+$ candidates within $\pm 2\sigma$ of the accepted D^+ mass. The K_s^0 mass resolution for events reconstructed in this region of the spectrometer is 4 MeV/c^2. There does not appear to be any K_s^0 decays present in this sample.

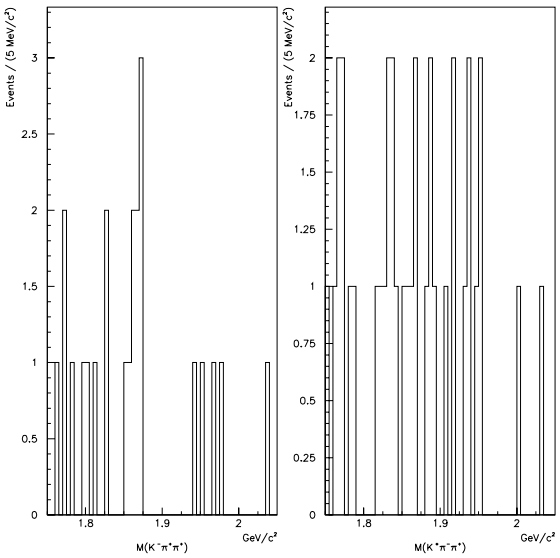

Figure 5.6: $D^+ \rightarrow K^-\pi^+\pi^+$ contamination in the $K^+\pi^-\pi^+$ invariant mass distribution. The left figure contains $K^-K^+\pi^+$ combinations from $K^+\pi^-\pi^+$ candidates within $\pm 2\sigma$ of the accepted D^+ mass. The right figure contains $K^-\pi^+\pi^+$ combinations from $K^-K^+\pi^+$ candidates within $\pm 2\sigma$ of the D^+.

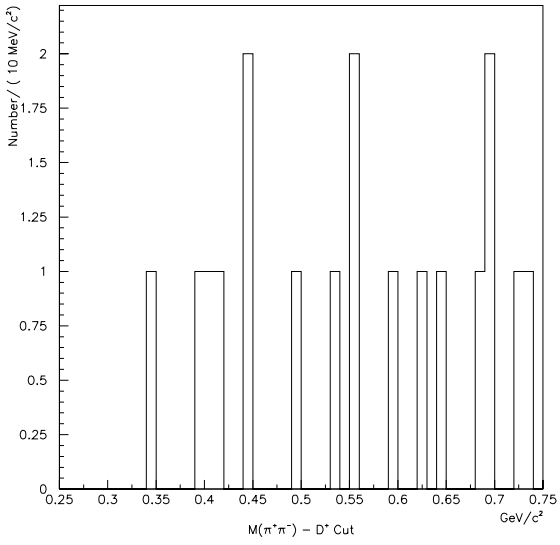

Figure 5.7: The $\pi^+\pi^-$ invariant mass distribution from $K^+\pi^-\pi^+$ events having a $K^+\pi^-\pi^+$ invariant mass with $\pm 2\sigma$ of the accepted D^+.

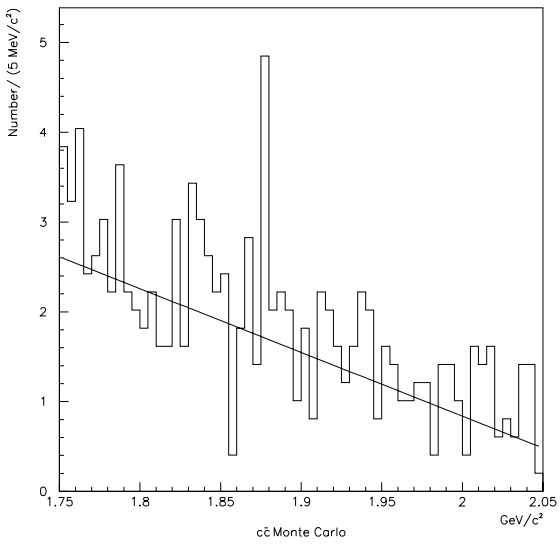

Figure 5.8: The $K^+\pi^-\pi^+$ invariant mass distribution from a $c\overline{c}$ Monte Carlo. The histogram has been scaled to represent the E-687 data set.

In an attempt to quantify the total contribution to the $K^+\pi^-\pi^+$ signal from all charm sources, a Monte Carlo sample was generated with all known charm and anticharm particles and also their known decay modes. The decay $D^+ \to K^+\pi^-\pi^+$ was not simulated in this sample. The total number of events generated corresponds to 4.9 times the E-687 data set. The sample was passed through the $K^+\pi^-\pi^+$ analysis stream, and Figure 5.8 shows $K^+\pi^-\pi^+$ invariant mass distribution for these events. The distribution has been scaled to represent the E-687 data set. The distribution was fit with a single Gaussian added to a polynomial background shape. The D^+ yield is 0.0 ± 4.4 events.

5.3.4 Branching Ratio Results

Using the fit results from Figure 5.3, the branching ratio,

$$\frac{, (D^+ \rightarrow K^+\pi^-\pi^+)}{, (D^+ \rightarrow K^-\pi^+\pi^+)} = 0.0072 \pm 0.0023, \quad (5.3)$$

is measured. It is found that the Monte Carlo efficiencies for both states are nearly identical and therefore cancel in the ratio. This measurement is preliminary as systematic uncertainties have not been considered yet. To check the validity of this measurement, the various cut parameters were varied and the stability of the branching ratio checked.

Figure 5.9 demonstrates the stability of the branching ratio as the ℓ/σ_ℓ cut is varied. All points are statistically consistent with each other demonstrating the proper lifetime evolution of the $K^+\pi^-\pi^+$ candidates.

Figure 5.10 shows the stability of the branching ratio as the ISO1 and ISO2 cuts are varied. The data were subjected to increasing levels of significance of cut as the branching ratio is plotted from left to right. Each study required that either the ISO1 or ISO2 cut be less than some value. The values used, as the study number increased, for the ISO1 studies were: 100%, 50%, 15%, 5%, 1%, 0.1%, 0.01%, and 0.0001%. The ISO2 cut values used: 100%, 1%, 0.1%, 0.01%, 0.001% 0.0001%. It is apparent that the ISO1 cut experiences a turn on point at around 1%. This is due to the background present in data which affects the signal to noise of the mass peak. Data and Monte Carlo Studies using the Cabibbo favored $K^-\pi^+\pi^+$ decay show that

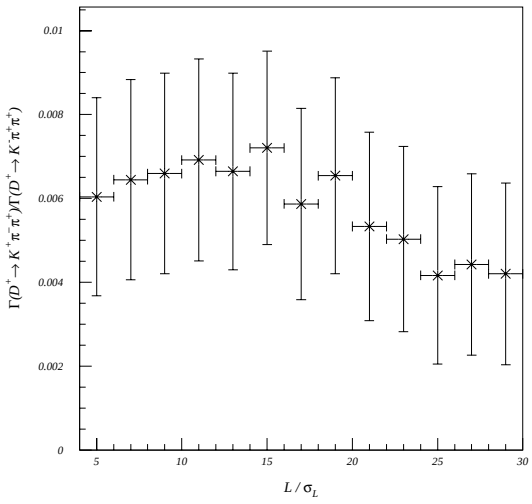

Figure 5.9: Variation of the $K^+\pi^-\pi^+$ branching ratio with ℓ/σ_ℓ.

the ISO1 cut is well understood, as will be seen in the $D_s^+\to\phi\pi^+$ signal. Aside from the dip at low significance of ISO1 cut, the branching ratio appears stable over a large range (6 orders of magnitude) of both ISO1 and ISO2 cuts.

Figure 5.11 shows the stability of the branching ratio as the position of the decay vertex is moved. Each study required that ℓ_v/σ_{ℓ_v} be greater than some value. Since, ℓ_v/σ_{ℓ_v} is the statistical separation from the downstream end of the target, negative numbers represent decay vertices in the target. The corresponding cuts as the study number is increased were ℓ/σ_ℓ greater than: No cut, -30, -20, -10, -5, 1.5, 5, 10, and 20. Again the branching ratio shows good stability.

Finally, Figure 5.12 shows the stability of the branching ratio as the DCL cut is varied. Each study required that the decay vertex confidence level (DCL)

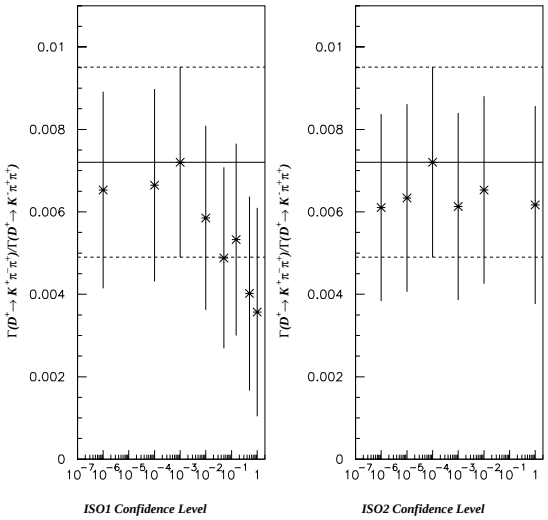

Figure 5.10: Variation of the $K^+\pi^-\pi^+$ branching ratio with ISO1 and ISO2 cuts. See text for details on the values used for each study.

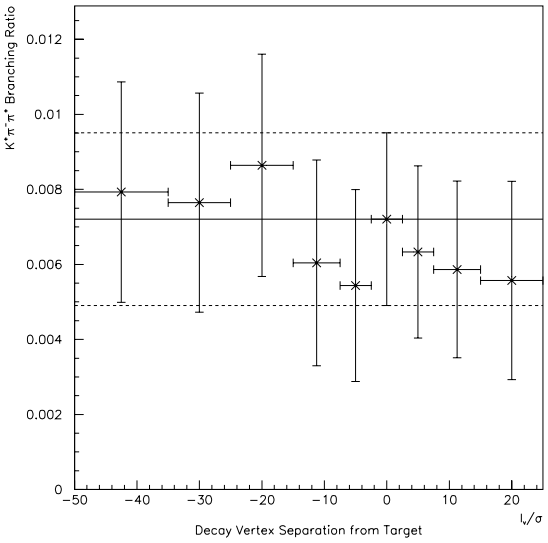

Figure 5.11: Variation of the $K^+\pi^-\pi^+$ branching ratio with the decay vertex position. See text for details on the values used for each study.

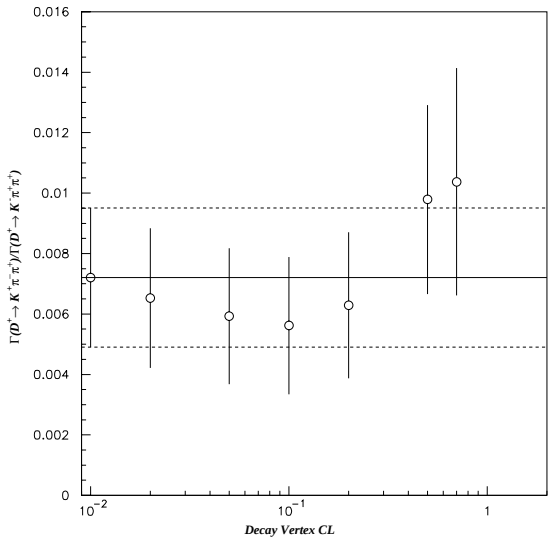

Figure 5.12: Variation of the $K^+\pi^-\pi^+$ branching ratio with the decay vertex confidence level (DCL). See text for details on the values used for each study.

be greater than the following values (with increasing study number): 1%, 2%, 5%, 10%, 20%, 50%, 70%.

5.3.5 Systematic Uncertainties

Despite the good agreement between the behavior of the $K^+\pi^-\pi^+$ and $K^-\pi^+\pi^+$ signals, there are still systematic uncertainties which must be considered in the measurement. Three sources of systematic uncertainty have been identified.

- The background shape used in the fit.
- Uncertainty in the efficiency calculation due to intermediate two-body resonant decay contributions to the inclusive signal.

- The amount of contamination from charm background sources.

The first contribution arises as a result of the uncertainty in the proper background shape used during the fit of the $K^+\pi^-\pi^+$ invariant mass distribution. To calculate this uncertainty, the $K^+\pi^-\pi^+$ distribution was refit many times, each time varying the conditions of the fit. The branching ratio was then recalculated and the mean and variance of the the resulting branching ratio distribution were calculated. The 1σ value for this distribution was used to estimate this systematic uncertainty. This value was determined to be 8.3% of the branching ratio presented above.

The second contribution to the systematic uncertainty arises due to ignorance of the intermediate states which might contribute to a $K^+\pi^-\pi^+$ final state. For example, the decay $D^+ \rightarrow K^{*0}(892)\pi^+$, where the K^{*0} decays into the $K^+\pi^+$ final state will contribute to the observed $K^+\pi^-\pi^+$ signal. Also contributing will be the decay $D^+ \rightarrow K^+\rho^0(770)$, where the ρ^0 decays into the $\pi^+\pi^-$ final state. As can be seen from Table 5.3, due to the variation in spectrometer acceptance across the $K^+\pi^-\pi^+$ Dalitz plot, there are variations in the integrated efficiencies for the states $K^{*0}\pi^+$, $K^+\rho^0$, and non-resonant $K^+\pi^-\pi^+$. To account for this variation, three branching ratios were calculated using the Monte Carlo efficiencies for each of these states. The mean and variance of these ratios were calculated, and the 1σ value was used for the systematic uncertainty. This systematic uncertainty was measured to

Table 5.3: Monte Carlo efficiencies for various $K^+\pi^-\pi^+$ decays.

Decay	Monte Carlo efficiency (%)
$D^+ \rightarrow K^+\pi^-\pi^+$ $n.r.$	1.20 ± 0.02
$D^+ \rightarrow K^{*0}\pi^+$	1.11 ± 0.02
$D^+ \rightarrow K^+\rho^0$	1.08 ± 0.02

be 5.6% of the branching ratio.

Finally, as was mentioned during the discussion regarding backgrounds, the uncertainty in the amount of charm contamination in the $K^+\pi^-\pi^+$ signal was 4.4 events. This represents a 21% uncertainty in the background contamination of the signal, and will be included in the systematic error.

Combining the systematic uncertainties, this leads to an inclusive branching ratio measurement of,

$$\frac{, (D^+ \rightarrow K^+\pi^-\pi^+)}{, (D^+ \rightarrow K^-\pi^+\pi^+)} = 0.0072 \pm 0.0023 \pm 0.0017. \quad (5.4)$$

5.3.6 Search for $D^+ \rightarrow K^{*0}(892)\pi^+$ and $K^+\rho^0(770)$ Decays

The $K^+\pi^-\pi^+$ final state can be fed by many sources, the most significant of which are expected to be $K^{*0}(892)\pi^+$, $K^+\rho^0(770)$, and non-resonant decays. Figure 5.13 shows the $K^+\pi^-$ and $\pi^+\pi^+$ invariant mass distributions for events which have passed the cuts outlined in the inclusive analysis. The figure shows slight evidence $\rho^0(770)$

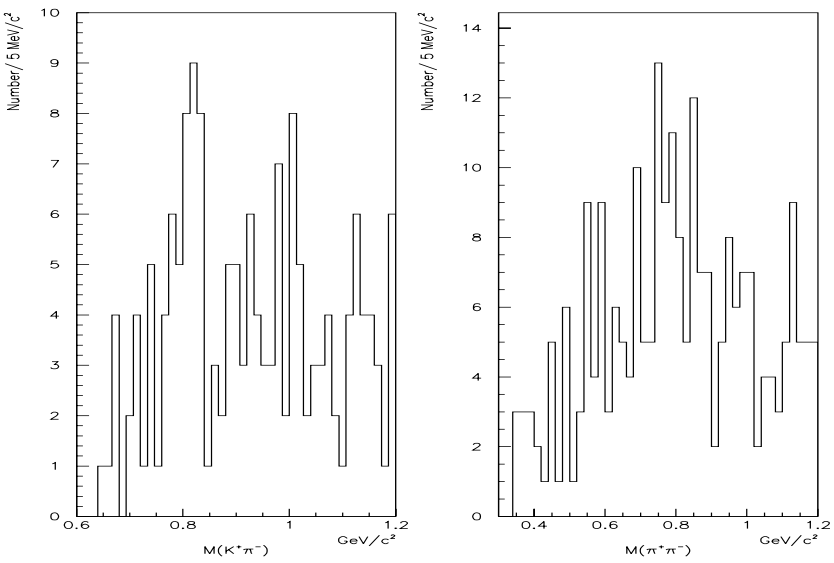

Figure 5.13: The $K^+\pi^-$ and $\pi^+\pi^-$ invariant mass distributions from $K^+\pi^-\pi^+$ data.

peak and no evidence for a K^{*0} signal. Figure 5.14 shows the Dalitz plot and projections for events falling within $\pm 2\sigma$ of the accepted D^+ mass. There does not appear to be any K^{*0} mass peak, and at best an ambiguous bump near the ρ^0 peak in the $\pi^+\pi^-$ projection.

Figure 5.15 shows the $K^+\rho^0$ and $K^{*0}\pi^+$ invariant mass distributions for the same cuts used in the inclusive analysis. The left plot requiring the $\pi^+\pi^-$ invariant mass to be within $\pm$, of the accepted $\rho^0(770)$ mass[1], where , is the accepted $\rho^0(770)$ natural width[1] of 150 MeV/c^2. To correct for other resonant or non-resonant $K^+\pi^-\pi^+$ decays, $K^+\pi^-\pi^+$ candidates having a $\pi^+\pi^-$ invariant mass falling in , wide mass windows centered ± 2.5, from the accepted $\rho^0(770)$ mass were subtracted. Since a significant portion of the D^+ signal resides in the long

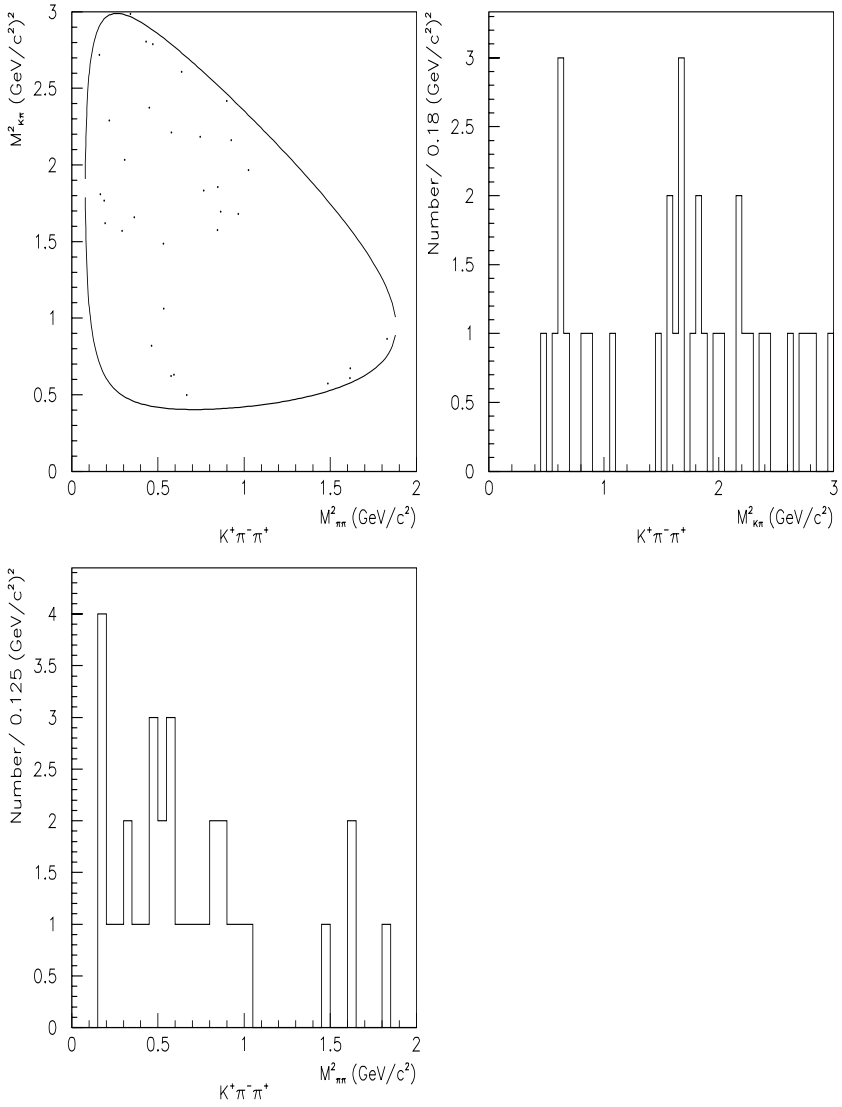

Figure 5.14: The $K^+\pi^-\pi^+$ Dalitz plot and $K^+\pi^-$, $\pi^+\pi^-$ mass projections.

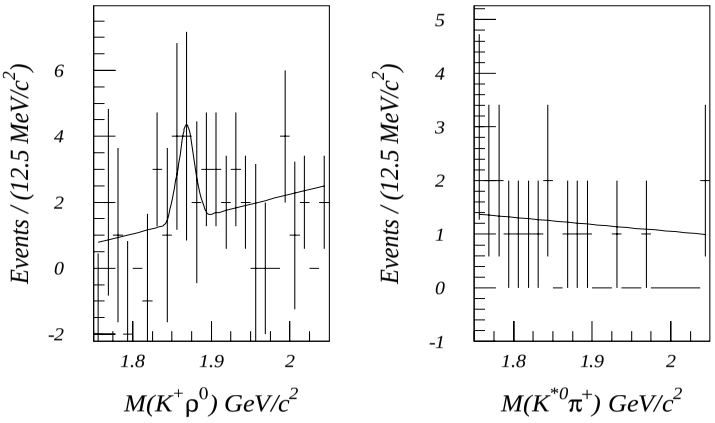

Figure 5.15: The $K^+\rho^0$ and $K^{*0}\pi^+$ invariant mass distributions for the D^+ analysis. The D^+ yields are: 5.8 ± 5.3 $K^+\rho^0$ and 0 ± 1 $K^{*0}\pi^+$ events.

Breit-Wigner tails of the resonance, a Monte Carlo sample was used to correct for D^+ events falling outside the , mass cut and and also to account for the D^+ events subtracted from the high and low mass windows. The right plot in Figure 5.15 shows the $K^+\pi^-\pi^+$ invariant mass distribution[1] where the $K^+\pi^-$ invariant mass was required to be within $\pm$, of the accepted $K^{*0}(892)$ mass[1], and again , is the accepted $K^{*0}(892)$ natural width[1] of 50 MeV/c^2. The invariant mass distributions were fit with single Gaussian peaks added to a polynomial background. The Gaussian means and widths were constrained to values determined from Monte Carlo studies. The D^+ yields are 5.8 ± 5.3 $K^+\rho^0(770)$ events and 0 ± 1 $K^{*0}(892)\pi^+$ events.

To calculate branching ratio upper limits for these decay modes, an integrated likelihood method was employed. The fit likelihood function is integrated with respect to all fit parameters and the 90% confidence level upper limit on the signal parameter $\mathcal{S}$ is determined by the condition

$$\frac{\int^{\mathcal{S}_{0.9}} d\mathcal{S} \int_{\Omega_{\vec{p}}} \prod_i dp_i \mathcal{L}(\vec{p})}{\int_{\Omega_{\mathcal{S}}} d\mathcal{S} \int_{\Omega_{\vec{p}}} \prod_i dp_i \mathcal{L}(\vec{p})} = 0.9 \tag{5.5}$$

where $\vec{p}$ is the vector of fit parameters (excluding $\mathcal{S}$) and $\Omega_{\mathcal{S}}$ and $\Omega_{\vec{p}}$ are the domains of $\mathcal{S}$ and $\vec{p}$. Using this method, the 90% confidence level upper limits on the number of $D^+ \to K^+\rho^0(770)$ and $K^{*0}(892)\pi^+$ events were found to be 14.4 and 2.8 respectively. The resulting Monte Carlo corrected upper limits are, , $(D^+ \to K^+\rho^0(770))/$, $(D^+ \to K^-\pi^+\pi^+) < 0.0067$ and , $(D^+ \to K^{*0}(892)\pi^+)/$, $(D^+ \to K^-\pi^+\pi^+) < 0.0021$, where the appropriate resonance decay branching ratios have been accounted for.

5.4 The $D_s^+ \to K^+\pi^-\pi^+$ Signal

5.4.1 Data Selection

The data for the $D_s^+ \to K^+\pi^-\pi^+$ analyses were gleaned from the same skim and used the same reconstruction techniques as described in the $D^+ \to K^+\pi^-\pi^+$ analyses.

[1] Due to the lack of statistics, events were not subtracted from this invariant mass distribution.

Since the lifetime of the D_s^+ is shorter than that of the D^+, it is necessary to apply an alternative set of cuts to obtain comparable rejections against backgrounds when searching for a $D_s^+ \to K^+\pi^-\pi^+$ signal. For example, the necessity of relaxing the decay length cut (ℓ/σ_ℓ) can be partially compensated for by requiring the magnitude of the $K^+\pi^-\pi^+$ three–momentum to be greater than some minimum value. This was found to preferentially remove background sources while being efficient for $D_s^+ \to K^+\pi^-\pi^+$ events. Figure 5.16 shows a study similar to the D^+ sensitivity studies. On the abscissa, the relative yield error is plotted and the inverse of the "Signal to Noise" ratio is plotted on the ordinate. The locus of points in the upper right hand corner of the plot were generated using fairly standard E-687 cut values. The kaon **ISTATP** values were required to be KP7, while the pions were required to be NHE (see Table 5.2 for explanation of these mnemonics). The isolation confidence levels of the production and decay vertices, ISO1 and ISO2, were not allowed to exceed 85% and 1% respectively. This set of cuts does not diminish the power of the ℓ/σ cut. They also do not provide much statistical significance. Vastly improved significance is achieved by increasing the significance of the primary isolation cut. The cuts used for the D_s^+ analysis are listed in Table 5.4.

Using these cuts, the $K^+\pi^-\pi^+$ invariant mass distribution is plotted in Figure 5.17 for both data and a $D_s^+ \to K^+\pi^-\pi^+$ Monte Carlo. The distribution was fit with two Gaussians added to a polynomial background. Unlike the D^+ analysis, the Gaussian means and widths were allowed to vary, with the exception of the D^+

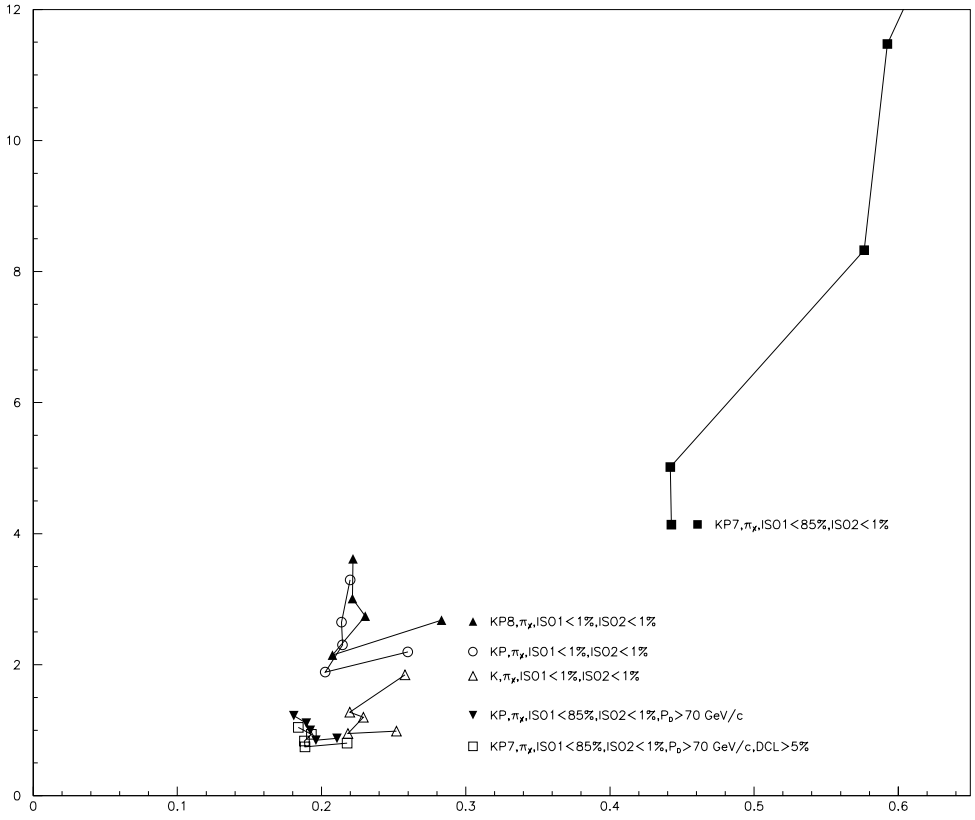

Figure 5.16: The relative error on the $D_s^+ \to K^+\pi^-\pi^+$ yield and inverse of "Signal to Noise" for various cuts. The trajectories represent increasing the ℓ/σ cut through the values, 5.0, 7.5, 10.0, 12.5, 15.0.

Table 5.4: Cuts used for $D_s^+ \to K^+\pi^-\pi^+$ analysis.

Cut	Value
Kaon	KP
Pions	$\neq 1, 4, 8, 12$
Prim. Mult	≥ 2 μ-strip Tracks
Secondary	No Double Links
PCL	$> 1\%$
DCL	$> 5\%$
ISO1	$< 1\%$
ISO2	$< 1\%$
P_D	$> 70 GeV/c$
ℓ/σ	> 10

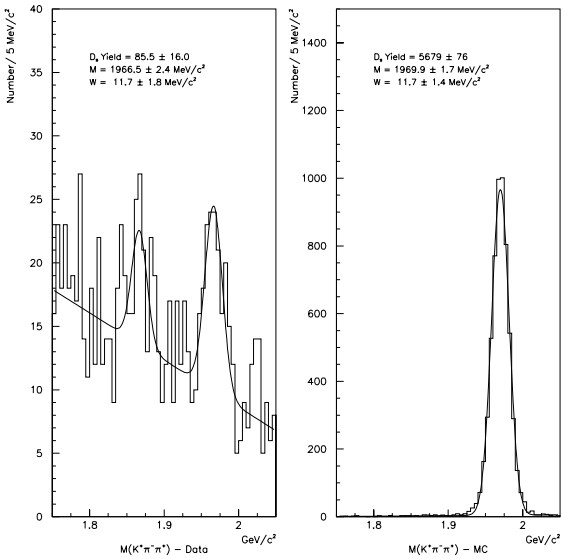

Figure 5.17: The $K^+\pi^-\pi^+$ invariant mass plots for data and Monte Carlo.

width. The D_s^+ yield is 85.5 ± 16.0 events the fit width agrees with the Monte Carlo width. Figure 5.18 shows the progression of the $K^+\pi^-\pi^+$ signal for various ℓ/σ_ℓ

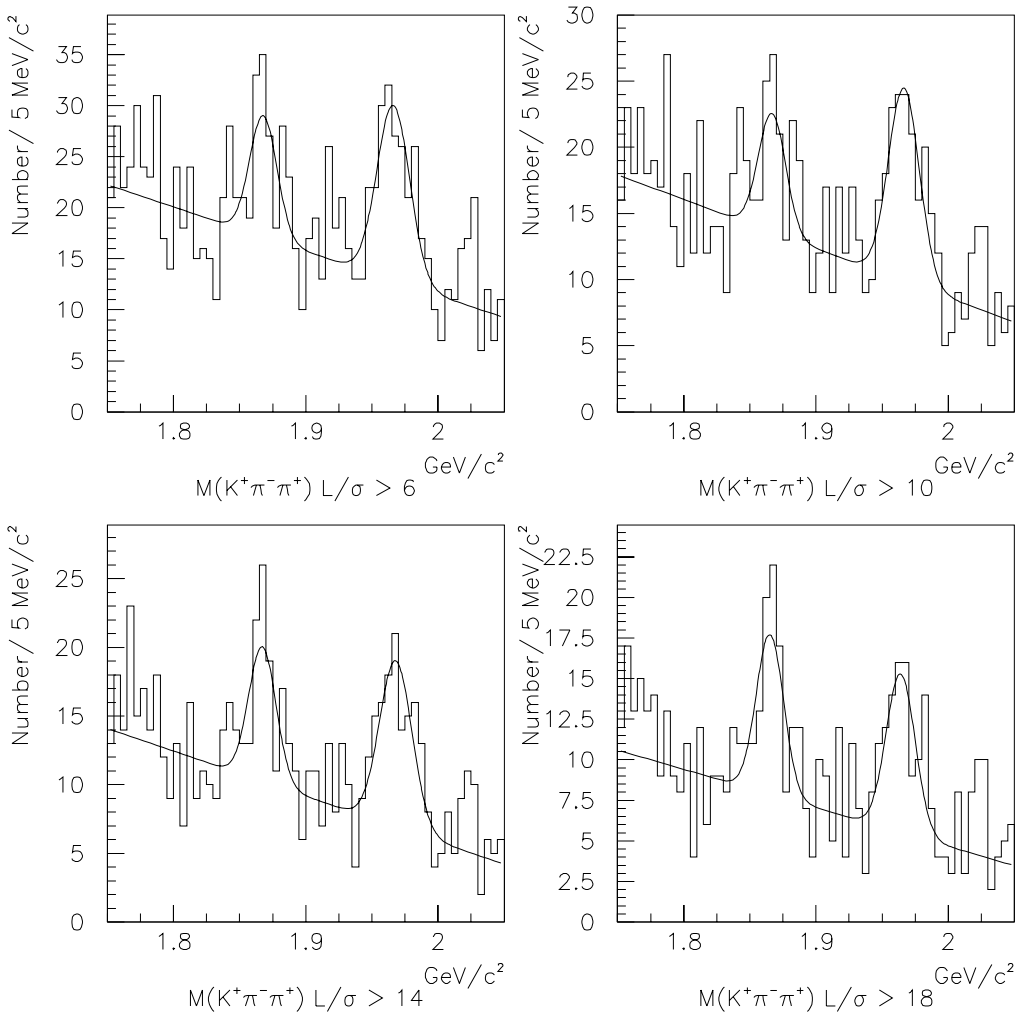

Figure 5.18: The $K^+\pi^-\pi^+$ invariant mass plots for various ℓ/σ cuts.

cuts.

5.4.2 Consideration of Backgrounds

As with the D^+ analysis there are several possible backgrounds which might contribute to the D_s^+ signal. One possible reflection background is $D^+ \to \pi^+\pi^-\pi^+$, where one of the π^+ particles is mis-identified as a K^+. The invariant mass would then be increased, thereby contributing near the D_s^+ mass region. To estimate the amount of this background, a large $D^+ \to \pi^+\pi^-\pi^+$ Monte Carlo was analyzed. Using this Monte Carlo to calculate the efficiency for reconstructing a $\pi^+\pi^-\pi^+$ decay in the D_s^+ analysis stream, and the accepted branching fractions for $D^+ \to K^-\pi^+\pi^+$, and $\pi^+\pi^-\pi^+$[1], the number of $\pi^+\pi^-\pi^+$ events expected in the D_s^+ signal region is calculated to be 1.7 ± 0.4. To check this calculation, the $\pi^+\pi^-\pi^+$ invariant mass distribution for both data and $K^+\pi^-\pi^+$ Monte Carlo events which have a $K^+\pi^-\pi^+$ invariant mass within 25 MeV/c^2 of the nominal D_s^+ are shown in Figure 5.19. The solid line is data, and the dashed line is Monte Carlo and the area has been normalized to data. The distributions are consistent with each other and the slight excess near the D^+ region is consistent with the above calculation. Since this contamination exists at the few percent level it will be included as a source of systematic uncertainty in the branching ratio measurement.

Another background to consider is $D_s^+ \to K_s^0 K^+$. As was the case for the D^+, this decay could be reconstructed in the analysis stream, if the K_s^0 were to decay immediately. This decay is not suppressed for the D_s^+. Figure 5.20 shows the $\pi^+\pi^-$

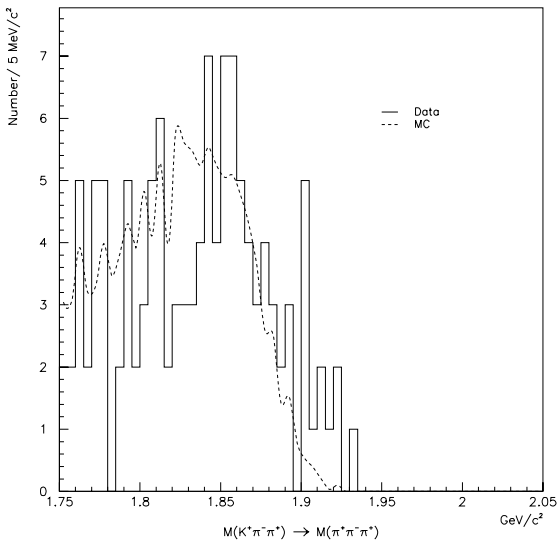

Figure 5.19: The $\pi^+\pi^-\pi^+$ invariant mass distributions for data and a $K^+\pi^-\pi^+$ Monte Carlo after passing through the $K^+\pi^-\pi^+$ analysis stream and having a $K^+\pi^-\pi^+$ invariant mass within 25 MeV/c^2 of the D_s^+. The solid line is data, the dashed Monte Carlo. The MC histogram was normalized to data.

invariant mass distribution for $K^+\pi^-\pi^+$ candidates within 2.5σ of the D_s^+ mass. There is no apparent accumulation of events near the K^0 mass.

Another check for contamination from charm backgrounds was performed by looking at the variation of the Monte Carlo corrected yield with ℓ/σ_ℓ. Figure 5.21 shows the results of this study as ℓ/σ_ℓ is varied from 6 to 26. This distribution demonstrates that the lifetime evolution of the $K^+\pi^-\pi^+$ candidates is consistent with the D_s^+ hypothesis.

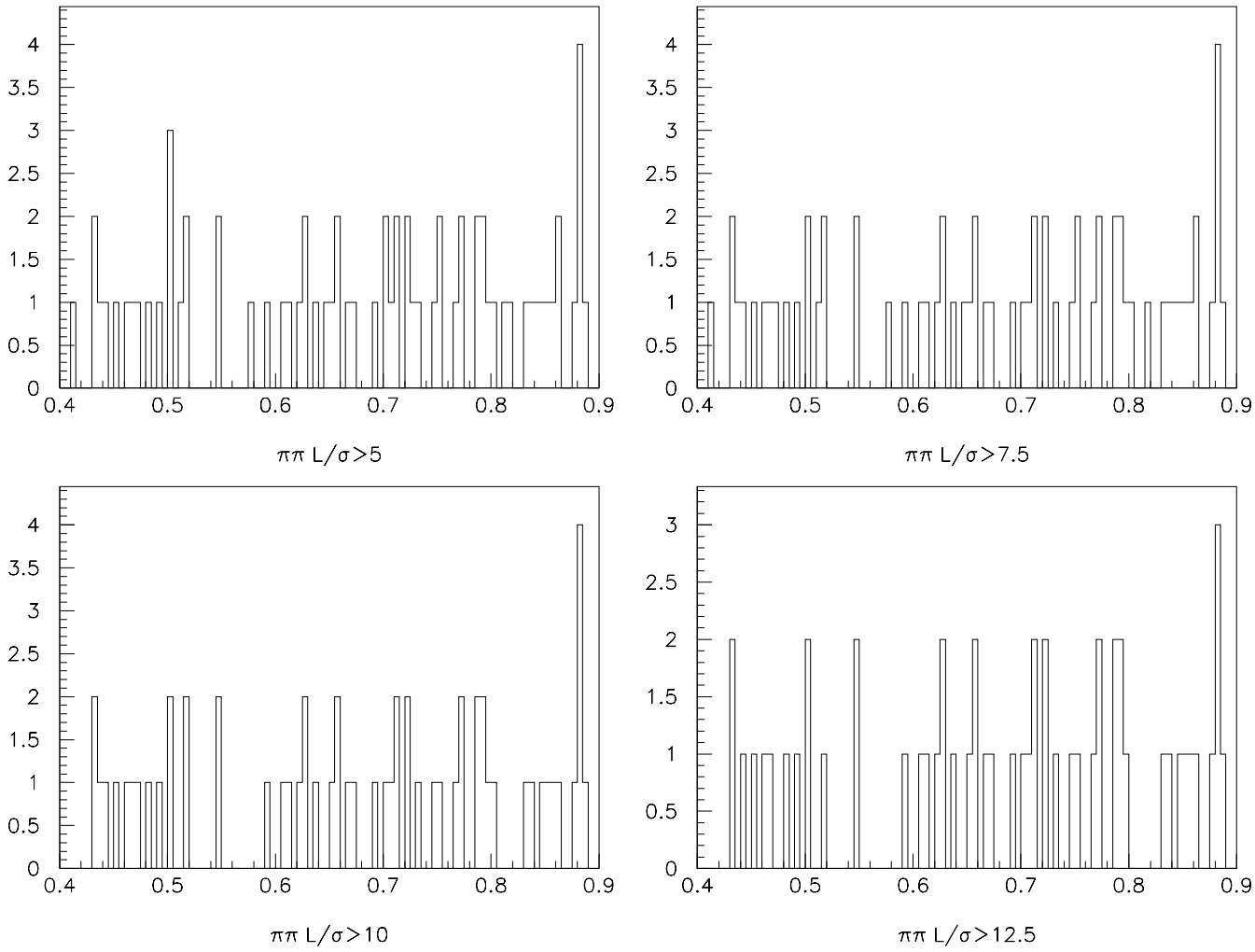

Figure 5.20: The $\pi^+\pi^-$ invariant mass for events with a $K^+\pi^-\pi^+$ mass within 2.5σ of the D_s^+

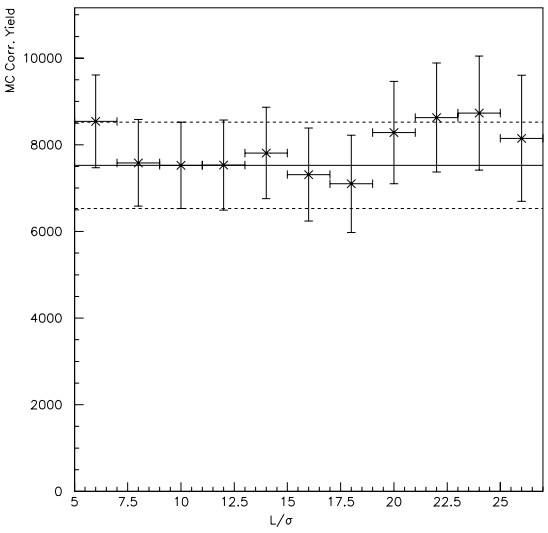

Figure 5.21: Variation of the Monte Carlo corrected yield with ℓ/σ_ℓ for the decay $D_s^+ \to K^+\pi^-\pi^+$.

5.4.3 Comparisons of D_s^+ Data with Monte Carlo

To further examine the quality of the signal, several comparisons between data and Monte Carlo generated events of various distributions were performed. Figure 5.22 shows the stability of the ISO1 and ISO2 cuts as the significance of the cuts is increased. The figure captions enumerate the values used for each study. Clearly the ISO1 cut does not become effective until the 1% level, but when this distribution is studied using the $\phi\pi^+$ signal, as shown in Figure 5.29, it is clear that the Monte Carlo correctly models data. From the right plot, it is also apparent that the ISO2 distribution is correctly modeled.

Figure 5.23 shows the comparison of the momentum distributions for data

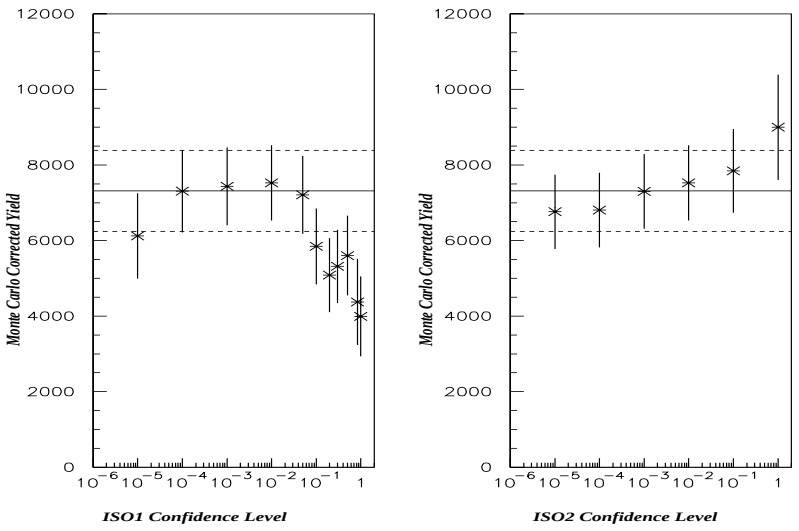

Figure 5.22: Comparison between D_s^+ data and Monte Carlo events of the ISO1 and ISO2 distributions. ISO1 studies 1-11 correspond to cuts of: $< 100\%$, $< 85\%$, $< 50\%$, $< 30\%$, $< 20\%$, $< 10\%$, $< 5\%$, $< 1\%$, $< 0.1\%$, $< 0.01\%$, 0.001% ISO2 studies 1-7 correspond to cuts of: 100%, 10%, 1%, 0.1%, 0.01%, 0.001%, 0.0001%

and reconstructed Monte Carlo events. The distributions have been normalized. The events were background subtracted using high and low mass windows starting 5.25 standard deviations from the accepted D_s^+ mass. The purpose of this subtraction was to statistically remove background events. The subtraction is accomplished by weighting events within ± 2.5 standard deviations of the measured D_s^+ mass with a value of 1, while events falling in ± 1.25 standard deviation wide windows described above were weighted by -1. The resulting figure shows the good agreement between the two distributions.

Figure 5.24 shows the comparison between various ISTATP categories for

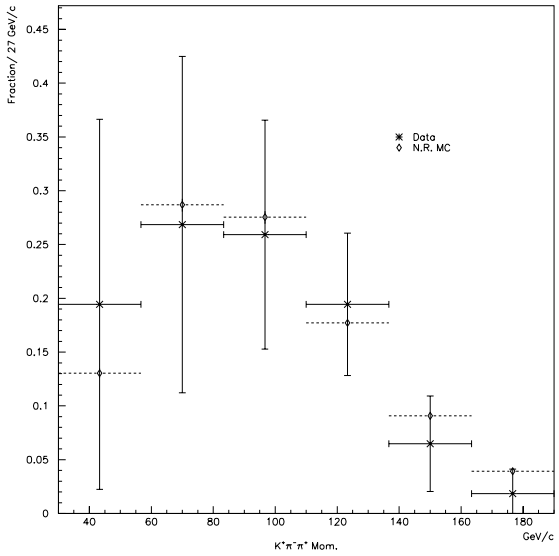

Figure 5.23: Comparison between D_s^+ data and Monte Carlo events of the D_s^+ momentum spectrum. The events were background subtracted using high and low mass windows (see text for details).

each of the daughter particles where the population of the mass histogram was large enough to fit. The agreement between these the two distributions is acceptable.

5.4.4 The $\phi\pi^+$ Signal

Data Selection

The signal used for normalization of the $K^+\pi^-\pi^+$ branching ratio is $D_s^+ \to \phi\pi^+$. The data used for the $\phi\pi^+$ signal were also collected from the skim described previously. To reduced the systematic uncertainties for this measurement, wherever a cut could be applied in the same manner as for the $K^+\pi^-\pi^+$ signal, this was done, with the

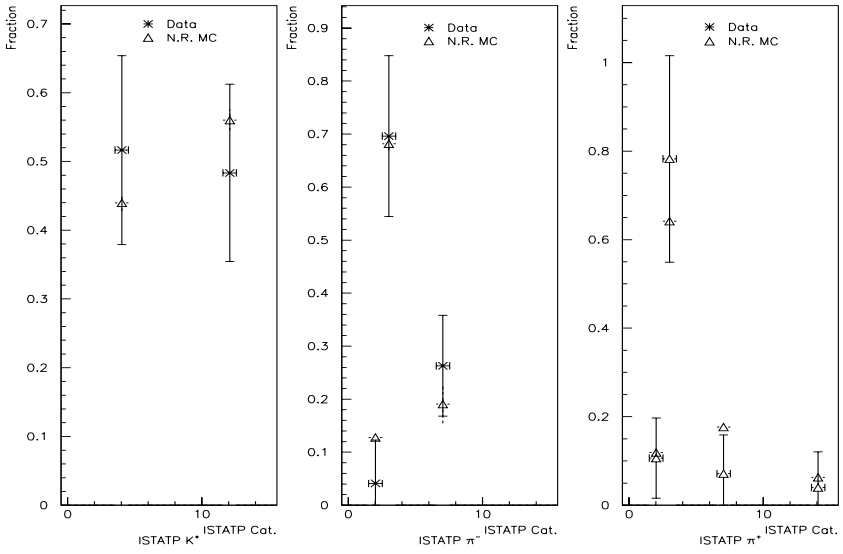

Figure 5.24: Data and Monte Carlo comparison of **ISTATP** category fractions for $D^+ \to K^+\pi^-\pi^+$ decays. Only categories where the mass plot was well populated were fit.

exception of ISO1. Since there are two kaons in the $\phi\pi^+$ final state, the requirements for the Čerenkov identification are slightly different, than for the $K^+\pi^-\pi^+$ signal. To reconstruct a ϕ candidate only the K^+ was required to be consistent with either a kaon or kaon/proton hypothesis, *i.e.* KP. The K^- track was allowed to have any possible **ISTATP** code. Figure 5.25 shows the resulting K^+K^- invariant mass distribution from $K^+K^-\pi^+$ candidate events passing the cuts listed in Table 5.4, but using the kaon Čerenkov identification requirements just described. The distribution was fit with a relativistic p-wave Breit-Wigner added to a simple polynomial. There are 345 ± 20 events in the Breit-Wigner peak.

The Čerenkov identification for pion candidates was the same as used in

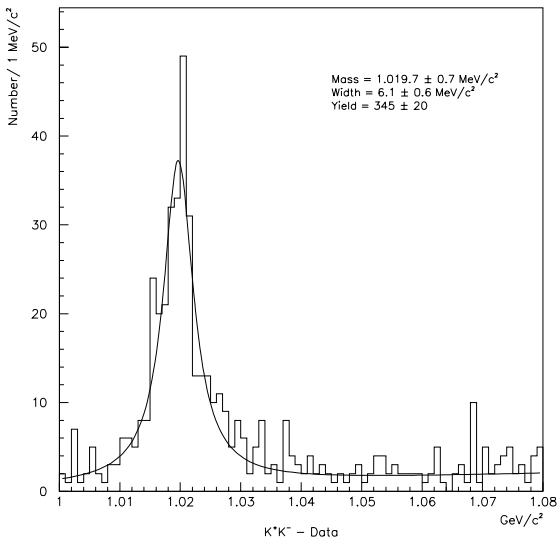

Figure 5.25: The K^+K^- candidates from the $K^+K^-\pi^+$ analysis using cuts described in the text. The measured mass and width are 1.0198 ± 0.0007 GeV/c^2, and 6.1 ± 0.6 MeV/c^2. The yield is 345 ± 20 events.

the $K^+\pi^-\pi^+$ signal, and for thoroughness, the full set of cuts used for the $\phi\pi^+$ signal are listed in Table 5.5. Combining this cut with a ± 1, mass cut on the ϕ candidates, Figure 5.26 shows the $K^+K^-\pi^+$ invariant mass distributions for both data and Monte Carlo. The figures include a ± 1, cut around the accepted ϕ mass, using the measured width, and the have been sideband subtracted in a manner similar to that described in the $D^+ \rightarrow K^+\rho^0(770)$ analyses. The evolution of the signal is demonstrated in Figure 5.27 which shows the mass peaks for various ℓ/σ_ℓ cuts.

Table 5.5: Cuts used for $D_s^+ \to K^+\pi^-\pi^+$ analysis.

Cut	Value
K^+	KP
K^-	No cut
π^+	$\neq 1, 4, 8, 12$
Prim. Mult	≥ 2 μ-strip Tracks
Secondary	No Double Links
PCL	$> 1\%$
DCL	$> 5\%$
ISO1	$< 50\%$
ISO2	$< 1\%$
P_D	$> 70 GeV/c$
ℓ/σ	> 10
$\lvert M_{K^-K^+} - M_\phi \rvert$	$< 2\sigma$

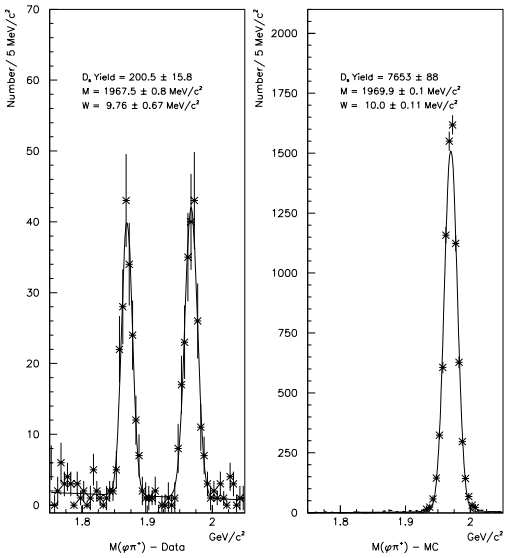

Figure 5.26: The $K^+K^-\pi^+$ data and Monte Carlo invariant mass distributions for normalization of the $K^+\pi^-\pi^+$ branching ratio. See text for details of cuts.

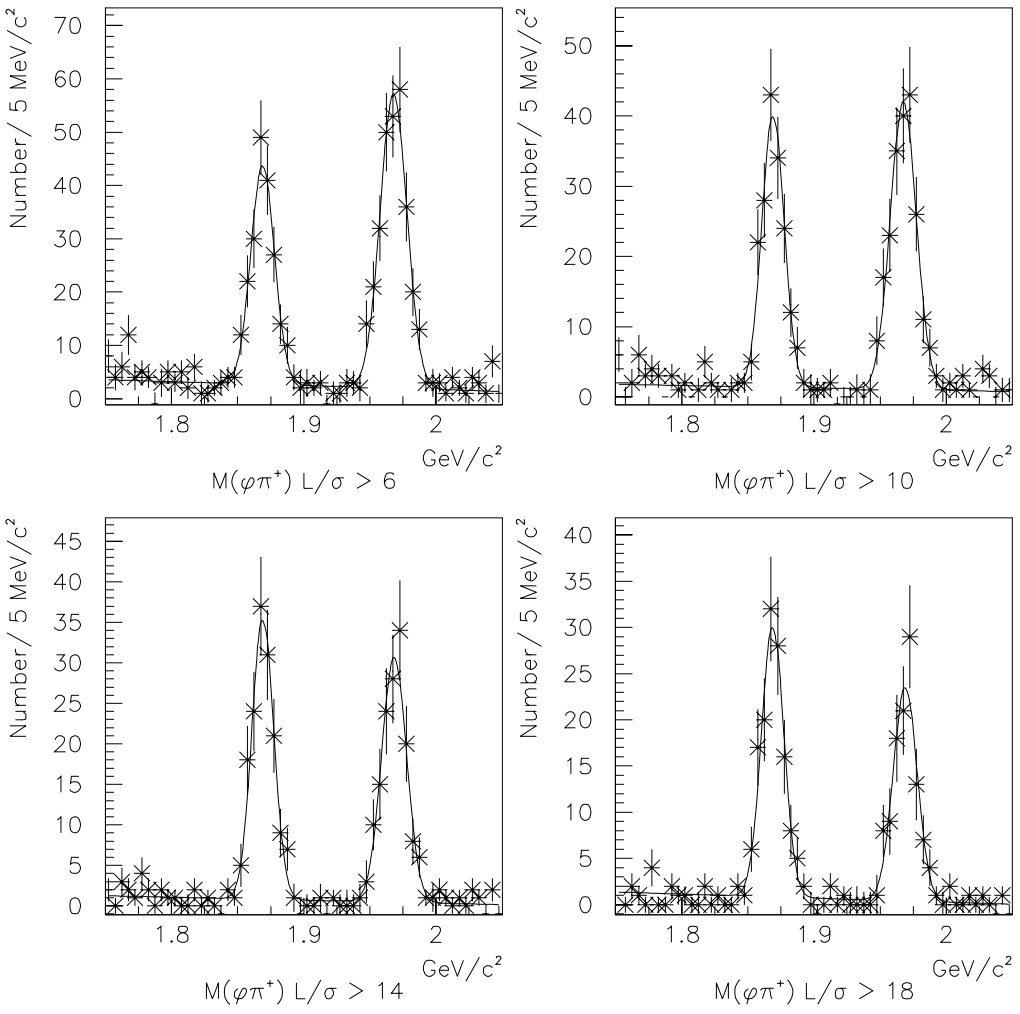

Figure 5.27: Progression of $K^+K^-\pi^+$ invariant mass distributions with ℓ/σ_ℓ.

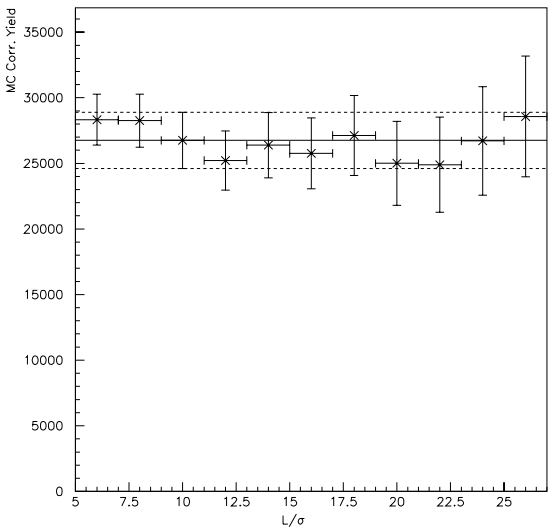

Figure 5.28: Stability of Monte Carlo corrected yield of $\phi\pi^+$ events vs. ℓ/σ_ℓ.

Comparisons with Monte Carlo

As with the $K^+\pi^-\pi^+$ signal, a large Monte Carlo sample of events was generated and passed through the $\phi\pi^+$ analysis stream. These events were then compared with data. Figure 5.28 demonstrates stability of the Monte Carlo corrected $\phi\pi^+$ yield as the ℓ/σ cut is varied.

Figure 5.29 shows the stability of the Monte Carlo corrected yield of the $\phi\pi^+$ events as ISO1 and ISO2 are varied. There appears to be excellent agreement between data and Monte Carlo for these two distributions. The cut values used for each study are the same as those listed in the $K^+\pi^-\pi^+$ studies.

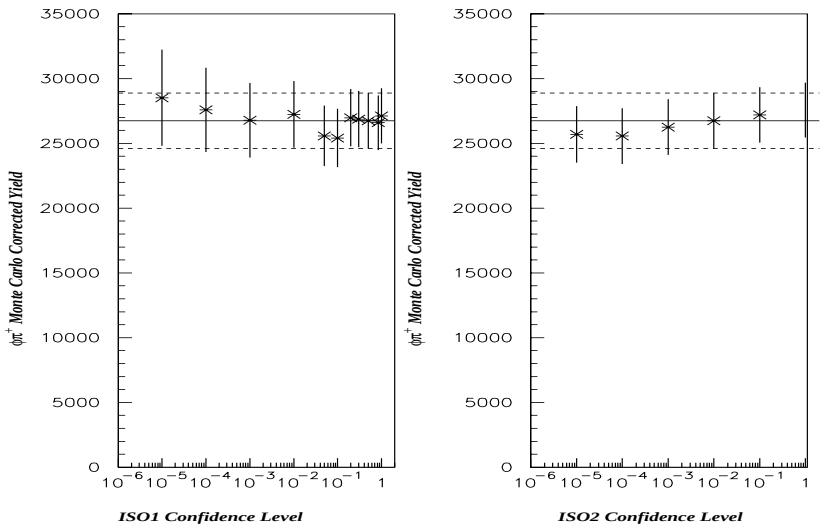

Figure 5.29: Monte Carlo corrected yields for $\phi\pi^+$ events vs. ISO1 and ISO2. Studies correspond to the same studies listed in the $K^+\pi^-\pi^+$ plot above.

Figure 5.30 shows the comparison between data and Monte Carlo momentum distributions. As in the $K^+\pi^-\pi^+$ case, the two spectra have been normalized and background subtracted. Although two data points appear to be slightly more than an error bar from the Monte Carlo data, the general trend appears to be in good agreement. This disagreement, though, will merit inclusion as a systematic uncertainty.

Figure 5.31 shows the comparison of the ISTATP distributions. Again, these distributions have been normalized and are background subtracted. The agreement here is acceptable.

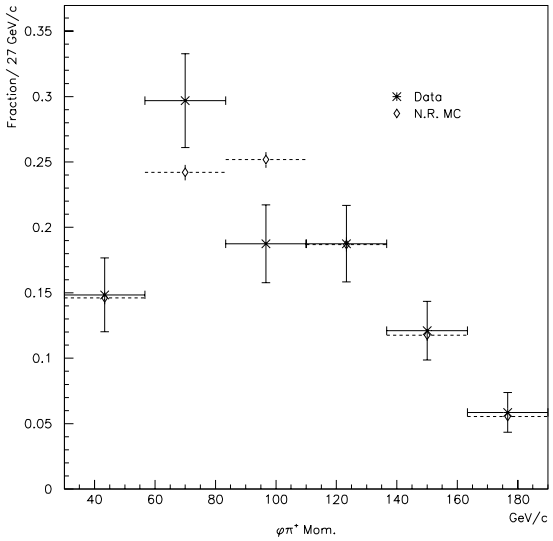

Figure 5.30: Comparison between data and Monte Carlo of background subtracted momentum spectra for $\phi\pi^+$ events.

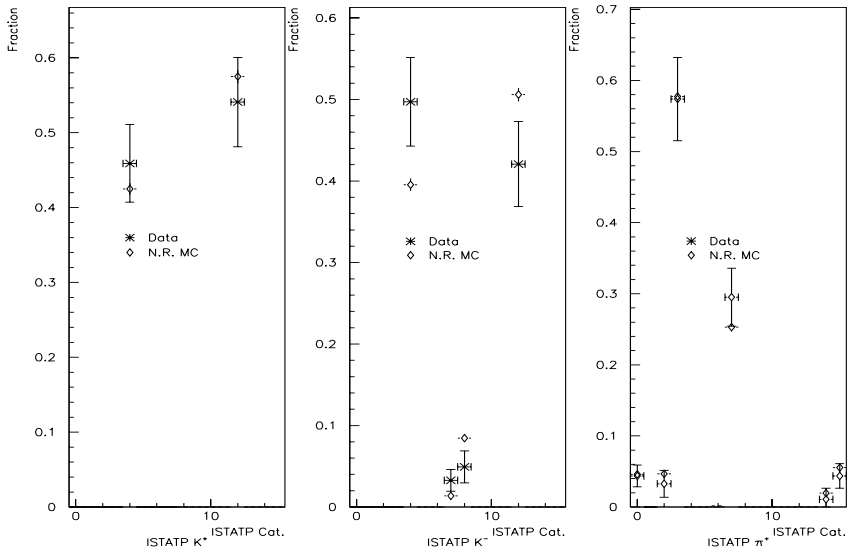

Figure 5.31: Data and Monte Carlo comparison of **ISTATP** category fractions for each daughter in $D_s^+ \to \phi\pi^+$ decays. The distributions have been background subtracted.

Table 5.6: Signal Yields and Efficiencies for $D_s \to K^+\pi^-\pi^+$, and $\phi\pi^+$

Signal	Yield	Monte Carlo Eff.
$K^+\pi^-\pi^+$	85.5 ± 16.0	0.0114
$\phi\pi^+$	200.5 ± 15.8	0.0153

5.4.5 Branching Ratio Results

Using the signals above and the yields and efficiencies are listed in Table 5.6, the preliminary branching ratio is

$$\frac{, (D_s \to K^+\pi^-\pi^+)}{, (D_s \to \phi\pi^+)} = 0.28 \pm 0.06,$$

where the accepted value for the branching fraction of $\phi \to K^+K^-$ was used.

5.4.6 Systematic Errors

There are four sources of systematic error which have been shown to contribute to the systematic uncertainty in the branching ratio. These sources are listed below.

- The background shape used in the fit.
- $D^+ \to \pi^+\pi^-\pi^+$ contamination.
- Modeling of the D_s^+ momentum spectrum.
- Uncertainty in the efficiency calculation due to intermediate two-body resonant decay distributions.

The systematic error associated with fitting was calculated in the D^+ analysis and amounts to 8.3% of the branching ratio.

Contamination in the D_s^+ peak from mis-identified $D^+ \to \pi^+\pi^-\pi^+$ events was calculated to be 1.7 ± 0.4 events. To account for this source of uncertainty, 2.3% of the branching ratio will be added in quadrature to the systematic error bar.

To calculate the systematic error associated with the poor matching of the momentum distributions, the data were broken into high and low momentum samples, *i.e.* $P_D < 90$ GeV/c^2, and $P_D > 90$ GeV/c^2. Figure 5.32 shows the two $K^+\pi^-\pi^+$ mass plots used for this study. The branching ratio for each sample was then calculated along with the χ^2 of the two independent measurements. The error on the mean of the two samples was then scaled by the χ^2 and compared to the fit error. Since it was larger than the fit error, the quadrature difference between the scaled error and the fit error was calculated and used as the systematic uncertainty associated with the momentum distribution. This uncertainty was measured to be 16% of the branching ratio.

The systematic uncertainty associated with the lack of knowledge of the contribution to the $K^+\pi^-\pi^+$ signal from two-body intermediate resonant decays is demonstrated by Table 5.7. Since the exact composition of the signal is unknown, there is some uncertainty in the correct Monte Carlo efficiency to use. To account for this uncertainty, the branching ratio was calculated using each of the independent

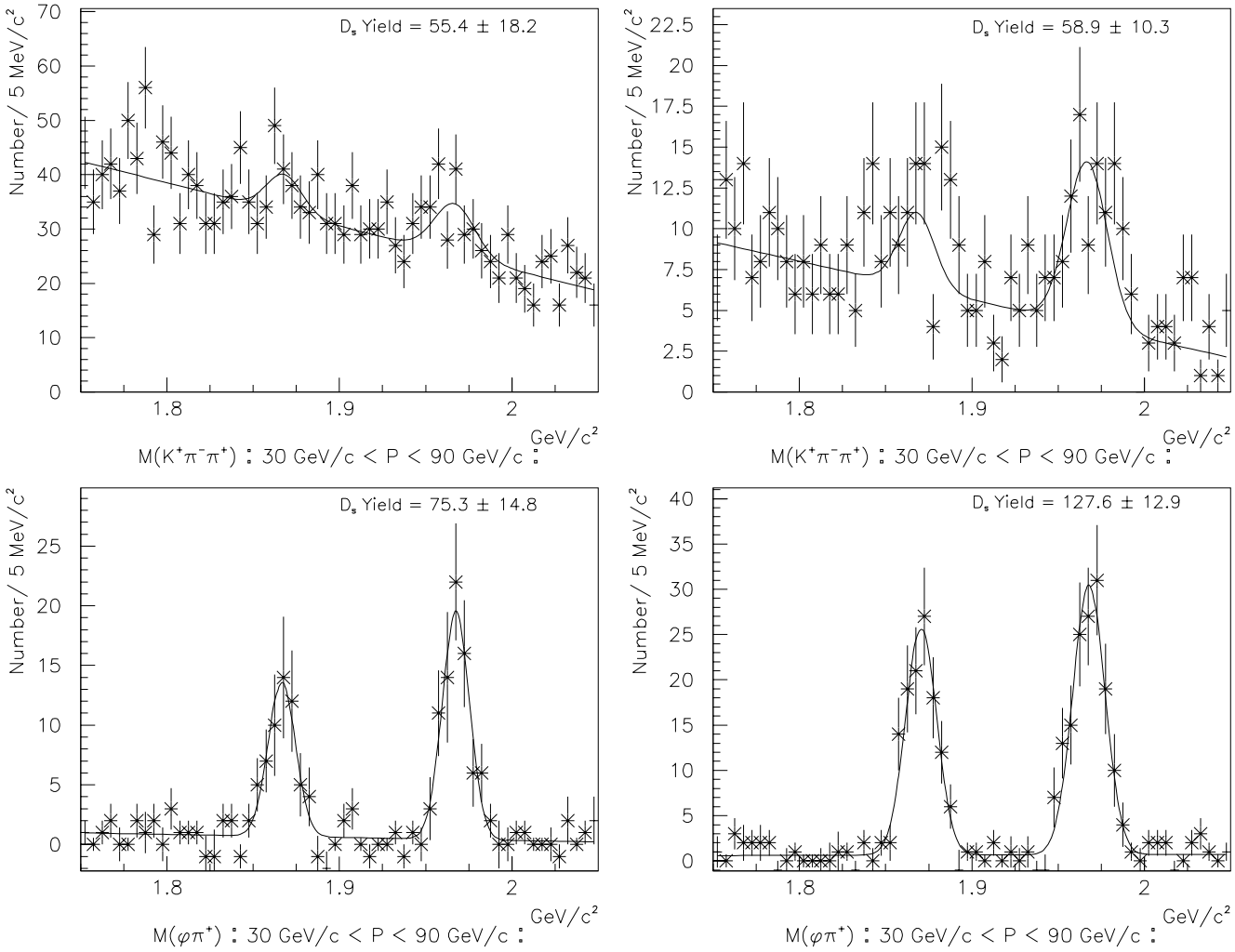

Figure 5.32: Mass plots used in the calculation of the systematic error associated with momentum.

Table 5.7: Monte Carlo efficiencies for $D_s^+ \to K^+\pi^-\pi^+$ n.r., $K^*0\pi^+$, $K^+\rho^0$.

Decay	Monte Carlo efficiency
$K^+\pi^-\pi^+$ n.r.	0.0114
$K^{*0}\pi^+$	0.0105
$K^+\rho^0$	0.0106

Table 5.8: Systematic Errors

Source	Magnitude	Fraction of B.R.
Fitting	0.023	8.3%
Contamination	0.007	2.3%
Momentum	0.045	15.9%
Matrix Element	0.016	5.6%

efficiencies and the variance on the mean of these measurements used to conservatively estimate this effect. This uncertainty is equal to 5.6% of the branching ratio.

In summary, four sources of systematic error have been calculated, fitting, $D^+ \to \pi^+\pi^-\pi^+$ contamination, D_s momentum, and knowledge of the $K^+\pi^-\pi^+$ matrix element. The magnitudes of each error are summarized in table 5.8.

Adding the systematic uncertainties in quadrature, the ratio of partial widths is measured to be,

$$\frac{, (D_s \to K^+\pi^-\pi^+)}{, (D_s \to \phi\pi^+)} = 0.28 \pm 0.06 \pm 0.05.$$

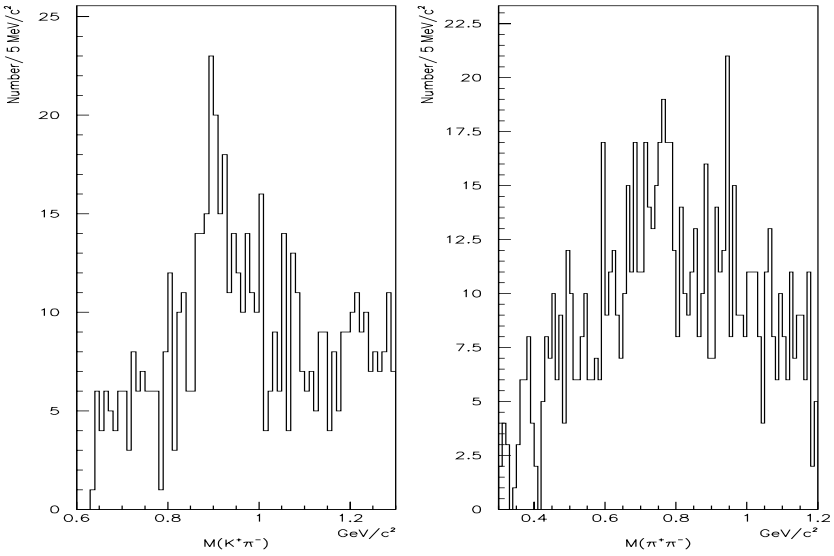

Figure 5.33: $K^+\pi^-$ and $\pi^+\pi^-$ invariant mass distributions for events in the $K^+\pi^-\pi^+$ analysis stream.

5.4.7 Searches for $D_s^+ \to K^{*0}(892)\pi^+$ and $K^+\rho^0(770)$.

Repeating the searches performed in the D^+ analysis, searches for two-body intermediate resonant decays were performed. Figure 5.33 shows the $K^+\pi^-$, and $\pi^+\pi^-$ invariant mass distributions for events which have passed the cuts outlined in the inclusive analysis. The figure shows clear K^{*0} and ρ^0 peaks in the data stream. Figure 5.34 shows the Dalitz plot and projections for events falling within $\pm 2\sigma$ (σ = 12.4 MeV/c^2) of the accepted D_s^+ mass. There appears to be a significant K^{*0} mass peak, and a less significant bump near the ρ^0 peak in the $\pi^+\pi^-$ projection.

Figure 5.35 shows the $K^+\pi^-\pi^+$ invariant mass distributions with ± 1, mass cuts on the $K^+\pi^-$ and $\pi^+\pi^-$ invariant masses about the accepted $K^{*0}(892)$ and

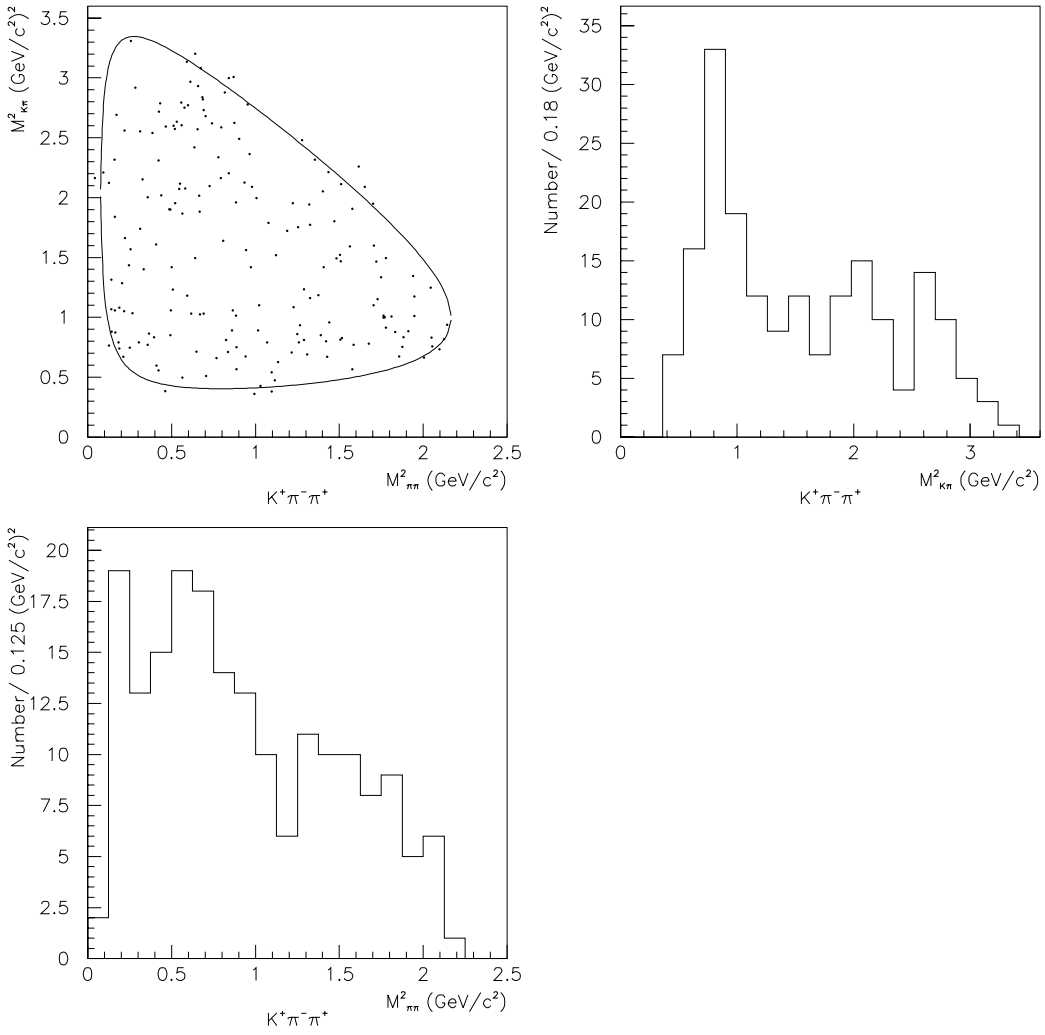

Figure 5.34: The $D_s^+ \to K^+\pi^-\pi^+$ Dalitz plot.

Table 5.9: Signal Yields and Monte Carlo efficiencies for $K^{*0}\pi^+$ and $K^+\rho^0$.

Decay	Yield	Monte Carlo efficiency	90% CL Upper Limit
$K^{*0}\pi^+$	24.7 ± 6.8	0.0075	-
$K^+\rho^0$	5.0 ± 9.8	0.0087	18.9

$\rho^0(770)$ masses. The data were subtracted as described above in the $D^+ \to K^+\rho^0$ analysis to account for other resonant and non-resonant decays contributing to the signal. The distributions were fit with Gaussian peaks added to polynomial background shapes. There appears to be a significant $K^{*0}\pi^+$ peak and slight evidence for a $K^+\rho^0$ peak. The D_s^+ yields are: 5.0 ± 9.8 $K^+\rho^0$ events and 24.7 ± 6.8 $K^{*0}\pi^+$ events. As a consistency check, the $K^+\pi^-$ and $\pi^+\pi^-$ invariant masses are plotted in Figure 5.36 for events falling from within ± 2 standard deviations of the accepted D_s. These events were also sideband subtracted using high and low mass regions around the D_s^+. Again, there is a clear K^{*0} peak and no evidence for a ρ peak. The distributions were fit with a relativistic p-wave Breit-Wigner shape added to a simple polynomial. The K^{*0} yield is consistent with the $K^{*0}\pi^+$ yield. Figure 5.37 shows the Monte Carlo mass plots for the $K^+\pi^-\pi^+$ distributions and Table 5.9 lists the yields and efficiencies for the decays.

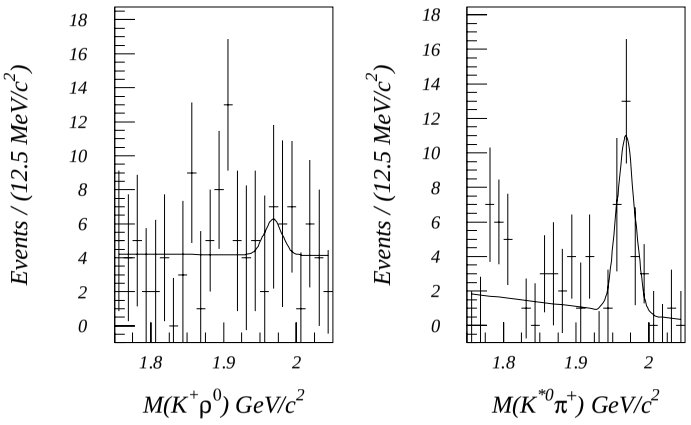

Figure 5.35: The $K^{*0}\pi^+$ and $K^+\rho^0$ background subtracted invariant mass distributions. The D_s^+ yields are: 5.0 ± 9.8 $K^+\rho^0$ events and 24.7 ± 6.8 $K^{*0}\pi^+$ events.

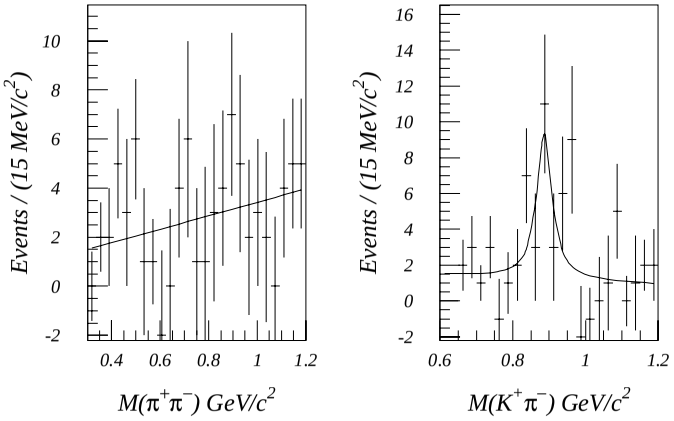

Figure 5.36: The $K^+\pi^-$ and $\pi^+\pi^-$ invariant mass distributions for $D_s^+ \to K^+\pi^-\pi^+$ events.

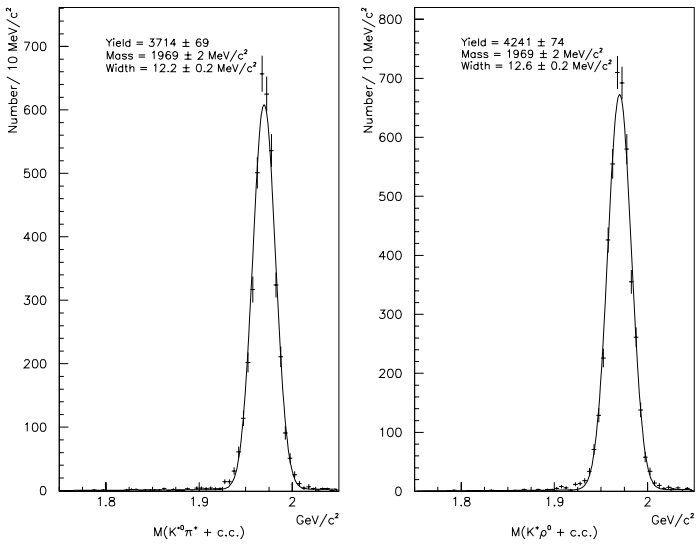

Figure 5.37: $K^{*0}\pi^-$ and $K^+\rho^-$ mass distributions from Monte Carlo.

5.4.8 $D_s^+ \to K^{*0}\pi^+$ and $K^+\rho^0$ Results

Since the $K^{*0}\pi^+$ signal is statistically significant from zero, a branching ratio was calculated. The preliminary ratio, where the resonance decay branching ratio has been included, is

$$\frac{, (D_s \to K^{*0}\pi^+)}{, (D_s \to \phi\pi^+)} = 0.18 \pm 0.05.$$

Once again the systematic uncertainties discussed in the inclusive analysis must be considered, with the exception of the uncertainty in which Monte Carlo efficiency to use. This gives a branching ratio of,

$$\frac{, (D_s \to K^{*0}\pi^+)}{, (D_s \to \phi\pi^+)} = 0.18 \pm 0.05 \pm 0.04,$$

Since the $K^+\rho^0$ signal is consistent with zero, an upper limit at 90% confidence level is calculated as described in the D^+ analyses. The upper limit at 90% confidence level on the number of events in this channel is calculated to be 18.9 events, which implies a branching ratio upper limit of

$$\frac{, (D_s \to K^+\rho^0)}{, (D_s \to \phi\pi^+)} \quad < \quad 0.08.$$

Chapter 6

Conclusion

Results of searches for doubly Cabibbo suppressed D^+ decays and singly Cabibbo suppressed D_s^+ decays using the $K^+\pi^-\pi^+$ final state have been reported. Evidence for the decay mode $D^+ \to K^+\pi^-\pi^+$ is observed and the branching ratio Relative to $D^+ \to K^-\pi^+\pi^+$ has been presented. Preliminary results for this decay mode have also been reported by Fermilab experiment E-791[34]. The inclusive ratio presented is , $(D^+ \to K^+\pi^-\pi^+)/$, $(D^+ \to K^-\pi^+\pi^+) = (7.2 \pm 2.3 \pm 1.7) \times 10^{-3}$. The previously published upper limit of 5% was reported in reference [2]. Also presented were branching ratio upper limits, at 90% confidence level, for the intermediate two-body resonant decay modes $D^+ \to K^{*0}(892)\pi^+$ and $D^+ \to K^+\rho^0(770)$ relative to $D^+ \to K^-\pi^+\pi^+$. The limits are , $(D^+ \to K^+\rho^0(770))/$, $(D^+ \to K^-\pi^+\pi^+) <$ 0.0067 and , $(D^+ \to K^{*0}(892)\pi^+)/$, $(D^+ \to K^-\pi^+\pi^+) < 0.0021$ Using the accepted branching fraction[1], , $(D^+ \to K^-\pi^+\pi^+) = 0.091 \pm 0.006$ the following branching

Table 6.1: Results of branching ratio measurements.

Branching Ratio	Result
$\frac{\Gamma(D^+\to K^+\pi^-\pi^+)}{\Gamma(D^+\to K^-\pi^+\pi^+)}$	$= (7.2 \pm 2.3 \pm 1.7) \times 10^{-3}$
$\frac{\Gamma(D^+\to K^{*0}(892)\pi^+)}{\Gamma(D^+\to K^-\pi^+\pi^+)}$	< 0.0021
$\frac{\Gamma(D^+\to K^+\rho^0(770))}{\Gamma(D^+\to K^-\pi^+\pi^+)}$	< 0.0067
$\frac{\Gamma(D_s^+\to K^+\pi^-\pi^+)}{\Gamma(D_s^+\to \phi(1020)\pi^+)}$	$= 0.28 \pm 0.06 \pm 0.05$
$\frac{\Gamma(D_s^+\to K^{*0}(892)\pi^+)}{\Gamma(D_s^+\to \phi(1020)\pi^+)}$	$= 0.18 \pm 0.05 \pm 0.04$
$\frac{\Gamma(D_s^+\to K^+\rho^0(770))}{\Gamma(D_s^+\to \phi(1020)\pi^+)}$	< 0.08

fraction upper limits are obtained, , $(D^+ \to K^+\rho^0(770)) < 6.1 \times 10^{-4}$, and , $(D^+ \to K^{*0}(892)\pi^+) < 1.9 \times 10^{-4}$.

Also included in this work is evidence for the decay mode $D_s^+ \to K^+\pi^-\pi^+$ and the first measurement of the branching ratio , $(D_s^+ \to K^+\pi^-\pi^+)/$, $(D_s^+ \to \phi(1020)\pi^+)$. The inclusive branching ratio is measured to be $0.28 \pm 0.06 \pm 0.05$. Evidence for the intermediate two-body resonant decay $D_s^+ \to K^{*0}(892)\pi^+$ is observed and the branching ratio , $(D_s^+ \to K^{*0}(892)\pi^+)/$, $(D_s^+ \to \phi(1020)\pi^+) = 0.18 \pm 0.05 \pm 0.04$ was presented. Finally, no signal was observed in the decay $D_s^+ \to K^+\rho^0(770)$ and the upper limit at 90% confidence level , $(D_s^+ \to K^+\rho^0(770))/$, $(D_s^+ \to \phi(1020)\pi^+) < 0.08$ was determined. All this is summarized

in Table 6.1.

As was mentioned in the introduction there are several theoretical approaches to studying non-leptonic charm decays. The $1/N_c$ expansion, the QCD Sum Rules, and the Heavy Quark Effective Theory approaches have all met with success at describing aspects of charm decays, but to date have not been able to make quantitative predictions regarding doubly suppressed D^+ and suppressed D_s^+ decays. Phenomenological models have been more successful in this endeavor. As was mentioned Chau and Cheng have made quantitative predictions for the doubly suppressed D^+ decay. This work finds the $K^+\rho^0(770)$ upper limit is 6 times the value predicted by Chau and Cheng, while the $K^{*0}(892)\pi^+$ upper limit is just twice the predicted value.

Since these limits are less than a factor of 10 away from these predictions, it appears that the next generation of charm physics experiments, *e.g.* Fermilab Experiment 831 will be able to measure these ratios at the levels predicted and provide new insights for these models and hopefully on the universe.

Bibliography

[1] Particle Data Group, L. Montanet et al., Phys. Rev. D 50 (1994)

[2] M. Piccolo et al Phys. Lett. **B 70** (1977) 260–263.

[3] J. C. Anjos et al Phys. Rev. Lett. **69** (1992) 2892–2895.

[4] M. Adamovich et al Phys. Lett. B **305** (1993) 177–181.

[5] D. Cinabro et al Phys. Rev. Lett. **72** (1994) 1406–1410

[6] S. Barlag et al Z. Phys. C **48** (1990) 29–45.

[7] S. Barlag et al Z. Phys. C **55** (1992) 383–390.

[8] A.J. Buras,J.-M. Gérard, and R. Rückl Nucl. Phys. B **268** (1986) 16–45.

[9] B. Yu. Blok and M.A. Shifman Sov. J. Nucl. Phys. **45** (1987) 135–142.

[10] B. Yu. Blok and M.A. Shifman Sov. J. Nucl. Phys. **45** (1987) 301–311.

[11] B. Yu. Blok and M.A. Shifman Sov. J. Nucl. Phys. **45** (1987) 522–531.

[12] B. Yu. Blok and M.A. Shifman Sov. J. Nucl. Phys. **46** (1987) 767.

[13] N. Isgur and M.B. Wise Phys. Lett. B **232** (1989) 113–117.

[14] N. Isgur and M.B. Wise Phys. Lett. B **237** (1990) 527–530.

[15] M.B. Voloshin and M.A. Shifman Sov. J. Nucl. Phys. **45** (1987) 463–466.

[16] M.B. Voloshin and M.A. Shifman Sov. J. Nucl. Phys. **47** (1988) 511–514.

[17] B. Grinstein Nuclear Physics B **339** (1990) 253–268.

[18] H. Georgi Phys. Lett. B **240** (1990) 447–450.

[19] I. I. Bigi, On Rare Decays of K, D and B Mesons *Proc. of the XVI SLAC Summer Institute on Particle Physics,* ed. by Eileen C. Brennan (Stanford University, Palo Alto, CA 1988).

[20] John Ellis, M.K. Gaillard, and D.V. Nanopoulos Nucl. Phys. B **100** (1975) 313–328.

[21] M.B. Voloshin, V.I. Zakharov, L.B. Okun JETP **21** (1975) 403–407.

[22] Dotcho Fakirov and Berthold Stech Nucl. Phys. B **133** (1978) 315–326.

[23] N. Cabibbo and L. Maiani Phys. Lett. B **73** (1978) 418–422.

[24] Manfred Bauer and Berthold Stech Phys. Lett. B **152** (1985) 380–384.

[25] Ling-Lie Chau, Hai-Yan Cheng Phys. Rev. Lett. **56** (1986) 1655–1658.

[26] M. Bauer, B. Stech, M. Wirbel *Z. Phys. C*, **34** 103 (1987)

[27] Ling-Lie Chau and Hai-Yang Cheng Phys. Rev. D **36** (1987) 137–153.

[28] Ling-Lie Chau and Hai-Yang Cheng Phys. Rev. D **42** (1990) 1837–1840.

[29] R.C. Verma and A.N. Kamal Phys. Rev. D **43** (1991) 829–842.

[30] K. Kodama et al. Phys. Lett. B **263** (1991) 573–578.

[31] Judd O'Hara Wilcox Ph. D. thesis, Univ. of California, Davis, (1992) 137–140.

[32] Glenn Richard Jaross Ph. D. thesis, Univ. of Illinois, Champaign-Urbana (1991) 127.

[33] Raymond Lloyd Culbertson Ph. D. thesis, Univ. of Illinois, Champaign-Urbana (1993) 54–72.

[34] M.V. Purohit et al. FERMILAB-Conf-94/186-E and FERMILAB-Conf-94/408-E (1994).